

# Rad21 is the core subunit of the cohesin complex involved in directing genome organization

**Yujie Sun** (✉ [sun\\_yujie@pku.edu.cn](mailto:sun_yujie@pku.edu.cn))

Biodynamic Optical Imaging Center (BIOPIC), Peking University <https://orcid.org/0000-0002-9489-4820>

**Yyao Sun**

Biodynamic Optical Imaging Center (BIOPIC), Peking University

**Xin Xu**

Peking University

**Wenxue Zhao**

Peking University

**Yu Zhang**

Tsinghua University

**Keyang Chen**

Peking University

**Yongzheng Li**

Peking University

**Xiaotian Wang**

Peking University

**Mengling Zhang**

Peking University

**Boxin Xue**

Peking University

**Wanting Yu**

Peking University

**Yingping Hou**

Peking University

**Chaobin Wang**

Peking University People's Hospital

**Wei Xie**

Tsinghua University <https://orcid.org/0000-0003-2126-3849>

**Cheng Li**

School of Life Sciences, Center for Bioinformatics, Center for Statistical Science, Peking University, Beijing <https://orcid.org/0000-0002-1766-1409>

**Daochun Kong**

Peking University

**Shu Wang**

Peking University People's Hospital

---

**Article**

**Keywords:**

**Posted Date:** December 14th, 2021

**DOI:** <https://doi.org/10.21203/rs.3.rs-1120640/v1>

**License:**   This work is licensed under a Creative Commons Attribution 4.0 International License.

[Read Full License](#)

---

GEO accession numbers:

The accession number is GSE183186 and reviewer token is "cjmromamlrefver".

1 **Full title: Rad21 is the core subunit of the cohesin complex involved in directing**  
2 **genome organization**

3 **Running title: Rad21 is core cohesin subunit directing genome organization**

4 Yua Sun<sup>1,\*</sup>, Xin Xu<sup>2,\*</sup>, Wenxue Zhao<sup>3,\*</sup>, Yu Zhang<sup>4</sup>, Keyang Chen<sup>5</sup>, Yongzheng Li<sup>1</sup>, Xiaotian  
5 Wang<sup>1</sup>, Mengling Zhang<sup>1</sup>, Boxin Xue<sup>1,6</sup>, Wanting Yu<sup>1</sup>, Yingping Hou<sup>7</sup>, Chaobin Wang<sup>8</sup>, Wei  
6 Xie<sup>4</sup>, Cheng Li<sup>3</sup>, Daochun Kong<sup>2</sup>, Shu Wang<sup>8</sup>, Yujie Sun<sup>1,8#</sup>

7 1 State Key Laboratory of Membrane Biology, School of Life Sciences, and Biomedical  
8 Pioneering Innovation Center (BIOPIC), Peking University, Beijing 100871, China

9 2 Peking-Tsinghua Center for Life Sciences, the National Laboratory of Protein and Plant  
10 Gene Research, College of Life Sciences, Peking University, Beijing, China.

11 3 Center for Bioinformatics, School of Life Sciences, Center for Statistical Science, Peking  
12 University, Beijing 100871, China

13 4 Center for Stem Cell Biology and Regenerative Medicine, MOE Key Laboratory of  
14 Bioinformatics, School of Life Sciences, THU-PKU Center for Life Science, Tsinghua  
15 University, Beijing 100084, China

16 5 Yuanpei College, Peking University, Beijing 100871, China

17 6 College of Chemistry and Molecular Engineering, Peking University, Beijing, China  
18 100871

19 7 Peking-Tsinghua Center for Life Sciences, Academy for Advanced Interdisciplinary Studies,  
20 Peking University, Beijing 100871, China

21 8 Breast Center, Peking University People's Hospital, Beijing 100044, China

22 \* These authors contributed equally to this work

23 # Corresponding author

24 Correspondence:

25 e-mail: sun\_yujie@pku.edu.cn (Y. Sun)

26 Phone number: 86-10-62744060

27 Cell number: 86-13051402289

28

29 **Abstract**

30 The ring-shaped cohesin complex is an important factor regulating genome structure. It is  
31 thought to mediate the formation of chromatin loops and topologically associating domains  
32 (TADs) by loop extrusion. However, the regulation of association between cohesin and  
33 chromatin is poorly understood. In this study, we directly visualized cohesin loading after  
34 up-regulation of cohesin subunit Rad21 by identifying the formation of vermicelli-like  
35 structures via live cell super-resolution imaging. We also reveal that cohesin loading can be  
36 promoted by Rad21-loader interactions and accumulated contacts were shown at TAD corners  
37 while inter-TAD interactions increased after vermicelli formation, indicating that Rad21 is an  
38 important determinant of chromatin structure. Moreover, we find that cohesin saddle on  
39 topologically associating domains by FISH assay, which is consistent with the  
40 CTCF/cohesin-anchored chromatin loop model. Importantly, expression of Rad21 is strictly  
41 controlled, and aberrant expression of Rad21 leads to the formation of Rad21 “beads” in the  
42 nucleus. In summary, our observations provided important new biological insights into the  
43 mechanism of cohesin loading and its functions.

44

## 45 **Introduction**

46 In eukaryotes, nuclear chromatin in the interphase is organized in a hierarchical manner.  
47 Previous studies using sequencing methods such as Hi-C detected genome-wide interactions,  
48 identified the plaid pattern of chromatin<sup>1</sup>, and divided chromatin into A and B compartments  
49 based on their different eigenvectors. The large compartments are composed of smaller TADs  
50 in the 0.2–1.0 Mb range, which are distinguished by the presence of more abundant  
51 intra-TAD interactions compared with inter-TAD interactions<sup>2</sup>. High-resolution Hi-C data  
52 revealed that chromatin within some TADs is organized into small, stable contact domains  
53 anchored by CTCF/cohesin, known as loop domains<sup>3,4</sup>.

54 The insulator protein CTCF and ring-shaped cohesin complex (also referred as “cohesin”  
55 below) were found to be located in the boundaries of TADs and loop domains<sup>2,3,5</sup>. In  
56 particular, it was demonstrated that CTCF and cohesin are important for the maintenance of  
57 loop domains using rapid protein depletion assays based on auxin-inducible degron tagging.  
58 These assays found a loss of insulation at most TAD boundaries after CTCF depletion while  
59 loop domains rapidly disappeared after cohesin degradation<sup>4,6</sup>. Previous studies have  
60 suggested that cohesin-DNA interaction plays an important architectural role in determining  
61 chromatin structure during the interphase. Multiple studies, including simulation, *in vitro*  
62 biochemical reconstitution, and single molecule imaging studies, have supported the loop  
63 extrusion model to explain the formation of loops and TADs as a process mediated by cohesin  
64 progressively extruding DNA until it encounters blocks formed by convergent dimeric  
65 CTCF<sup>7-12</sup>.

66 The cohesin complex was originally identified as a tripartite ring playing a role in sister

67 chromatid cohesion in the metaphase, which is constructed by the combination of a V-shaped  
68 SMC1/3 heterodimer and the kleisin subunit Rad21<sup>13,14</sup>. The association between chromatin  
69 and cohesin can be regulated by many factors. For example, cohesin antagonist Wapl can  
70 drive the release of cohesin from chromatin<sup>15-17</sup>. Tedeschi et al. depleted Wapl to stabilize the  
71 cohesin complex on chromatin and found a vermicelli-like distribution of chromatin,  
72 indicating that cohesin plays a role in chromatin condensation<sup>18</sup>. Moreover, high-resolution  
73 Hi-C data showed that chromatin loops are enlarged in cells with Wapl deficiency<sup>19</sup>,  
74 suggesting that the formation of the vermicelli-like distribution is likely caused by excessive  
75 chromatin extrusion with the help of over-loaded cohesin. Inversely, PDS5 is necessary for  
76 the maintenance of cohesin<sup>20</sup>. A loading complex called cohesin loader complex  
77 NIPBL-MAU2 (also known as SCC2/SCC4, respectively) is required for cohesin loading  
78 prior to DNA replication<sup>17</sup>. The loading complex is composed of the head, body and hook  
79 domains, and the latter two are sufficient to facilitate cohesin loading<sup>21</sup>. NIPBL was also  
80 shown to promote cohesin loading onto circular DNA topologically in vitro by direct  
81 interaction at multiple sites on cohesin subunits<sup>22</sup>. After the loading process, the loading  
82 complex is found to hop between different cohesin molecules rapidly in living cells<sup>23</sup>. Using  
83 cryo-electron microscopy, a recent study revealed the structure of cohesin bound to NIPBL  
84 and DNA, which provided the structural basis of cohesin-NIPBL-dependent DNA entrapment.  
85 However, the manner in which cohesin and NIPBL work cooperatively to promote chromatin  
86 condensation is unclear.

87 Here, we found that up-regulated expression of Rad21, but not other cohesin subunits,  
88 leads to excessive chromatin condensation with a vermicelli-like morphology. To investigate

89 the mechanism of cohesin loading and extrusion *in vivo*, we used super-resolution imaging  
90 and single-molecule imaging to measure the distribution of cohesin subunits. Fluorescence  
91 recovery after photo-bleaching and Co-IP results showed that Rad21-loader interaction  
92 promotes the formation of a vermicelli-like distribution by facilitating the cohesin loading  
93 process. Hi-C data showed that the short distance contact frequency increased in the presence  
94 of Rad21 up-regulation, while the long-distance contact frequency decreased. Upon Rad21  
95 up-regulation, chromatin interactions between A and B compartments increased and  
96 compartmentalization strength was reduced significantly. Correspondingly, accumulated  
97 contacts were shown at TAD corners and inter-TAD interactions increased. These  
98 observations support a cohesin loop extrusion model and lead us to propose the unique role of  
99 Rad21-loader interaction in cohesin loading and further cohesin extrusion. Moreover, we  
100 combined transcriptome changes and chromatin structure alterations upon Rad21  
101 up-regulation and revealed that Rad21 plays a role in breast cancer by affecting chromatin  
102 architecture.

103

## 104 **Results**

### 105 **Cohesin is arranged in axial chromosomal domains in cells with up-regulated Rad21**

106 To investigate the contributions of different cohesin subunits in the cohesin extruding process,  
107 we tagged the cohesin subunits SMC1A, SMC3, Rad21, SA1 and SA2 with HaloTag in HeLa  
108 cells. The HaloTag-fused cohesin subunits were fluorescently labeled by Janelia Fluor 549  
109 (JF549) in living cells and imaged by a super-resolution spinning disk confocal system (live  
110 SR CSU W1 Nikon). We observed that Rad21, as well as chromatin DNA, were both

111 arranged in a vermicelli-like pattern in cells upon Rad21 up-regulation (Fig. 1a and  
112 Supplementary information, Fig. S1a, b), suggesting that excessive Rad21 could cause  
113 chromatin DNA condensation. In contrast, over-expression (OE) of the other four cohesin  
114 subunits, SMC1A, SMC3, SA1 and SA2, resulted in even distributions (Supplementary  
115 information, Fig. S1c). The super-resolution images of the vermicelli pattern of Rad21  
116 revealed a “beads on a string” pattern (Fig. 1a), which indicates that Rad21 forms clusters on  
117 chromatin. Interestingly, the Rad21 “beads” were distributed regularly along chromatin with  
118 an average inter-bead distance of 0.34  $\mu\text{m}$  (Fig. 1b). To elucidate the relationship between  
119 vermicelli formation and up-regulated Rad21, we observed the distribution pattern of Rad21  
120 in live cells that expressed exogenous Rad21 over different time courses. The data showed  
121 that the extent of DNA condensation (Fig. 1c) was dependent on the expression level of  
122 Rad21. We also calculated the heterogeneity level, which revealed that the distribution of  
123 Rad21 became more heterogeneous as its expression level increased (Fig. 1d).

124 To examine whether Rad21 in the vermicelli are bound to chromatin, we performed  
125 inverted fluorescence recovery after photobleaching (iFRAP) experiments and observed that  
126 the fluorescence intensity of the unbleached region decayed very slowly (Fig. 1e, f). These  
127 results suggested that Rad21 binds stably on chromatin in the vermicelli.

128 To clarify the integrity of the cohesin ring structure bound to chromatin, SMC1A, SMC3  
129 and SA1 were immuno-stained in the absence and presence of Rad21 up-regulation. We found  
130 that endogenous H3 were distributed homogeneously, while SMC1A and SMC3 were  
131 colocalized with Rad21 and enriched in vermicelli-like structures after Rad21 up-regulation,  
132 which confirmed that the vermicelli-like distribution was caused by the whole cohesin

133 complex rather than Rad21 alone (Supplementary information, Fig. S1d and Fig. 1g, h). In  
134 addition, SA1 was less enriched in the vermicelli-like structures in comparison with SMC1A  
135 and SMC3, which is in line with the finding that SA1 does not participate in the construction  
136 of ring structures directly<sup>14,24</sup>. To further dissect the underlying molecular mechanism, we  
137 constructed three human Rad21 mutants (F597R, L601R and Q613K) (Supplementary  
138 information, Fig. S1e) that are unable to associate stably with SMC1/3 dimers as identified in  
139 fission yeast<sup>25</sup>. We found that none of the three Rad21 mutants could condense chromatin into  
140 vermicelli-like structures (Fig. 1i). Moreover, iFRAP led to a rapid decrease in the  
141 fluorescence intensity of the whole cell, indicating that these Rad21 mutants could not bind to  
142 chromatin without the formation of a cohesin complex (Supplementary information, Fig. S1f).  
143 Taken together, these results also suggest that formation of the vermicelli requires the whole  
144 cohesin complex.

145

146 **Rad21-loader interaction facilitates vermicelli-like structure formation by promoting**  
147 **cohesin loading**

148 The vermicelli-like phenotype observed upon Rad21 up-regulation could have two  
149 explanations. First, Rad21 may act as the limiting factor for cohesin formation so that  
150 up-regulation of Rad21 leads to an increased pool of cohesin. Alternatively, Rad21 may  
151 promote cohesin loading on chromatin and thus bias the loading/unloading balance of cohesin  
152 for excessive condensation of chromatin. To distinguish between these two possibilities, we  
153 performed salt extraction (Materials and Methods) to quantitatively measure the amount of  
154 cohesin that are mobile or bound weakly to chromatin (unloaded cohesin) and that bound

155 stably (loaded cohesin).

156 Western blotting data showed that up-regulation of Rad21 led to reduced expression of the  
157 endogenous Rad21 (Fig. 2a). Importantly, we found that the fraction of SMC3 bound to  
158 chromatin increased upon Rad21 up-regulation, while the fractions of bound and unbound  
159 Rad21 remain nearly unchanged (Fig. 2a, b). When cohesin complex were isolated from  
160 whole cell extract by immunoprecipitation against SMC3 in the present or the absent of  
161 Rad21 over-expression (Supplementary information, Fig. S2a), we found that up-regulation of  
162 Rad21 increased the amount of Rad21 by 2.5-fold while the total amount of cohesin showed  
163 almost no difference (Fig. 2c). Moreover, salt extraction and subsequent co-IP experiments  
164 showed that Rad21 up-regulation increased loaded cohesin, while the abundance of unloaded  
165 cohesin decreased (Fig. 2d). As shown in lanes 6 and 7, excessive Rad21 did not increase the  
166 proportion of cohesin in the unbound SMC3 pool. Considering that the amount of SMC3 with  
167 weak chromatin binding decreased, as shown in Fig. 2a, we inferred that up-regulated Rad21  
168 reduced the amount of unloaded cohesin. As shown in lanes 11 and 12, the proportion of  
169 cohesin in the chromatin-bound SMC3 pool was significantly elevated in Rad21-OE cells.  
170 These data collectively suggested that excessive Rad21 promoted cohesin loading on  
171 chromatin rather than increasing the abundance of the cohesin complex.

172 To further support the hypothesis that excessive Rad21 increases Rad21-loader interaction  
173 and thus promotes cohesin loading on chromatin, we constructed Rad21 mutants with  
174 disrupted interaction with the loader. Previous studies identified the Mis4Scc2–Ssl3Scc4  
175 interaction site between cohesin subunits in *S. pombe*<sup>22,26</sup>. To test this hypothesis in human  
176 cells, we constructed cells with Rad21-Loader-Interaction-Site (LIS) deletion and poly-Ala

177 mutations (Supplementary information, Fig. S2b). Salt extraction and subsequent co-IP  
178 experiments showed that LIS-Ala mutants accumulated more unbound Rad21 molecules in  
179 comparison with wild-type cells and Rad21 over-expressing HeLa cells, and also showed a  
180 lack of augmentation of cohesin loading without a significant difference in cohesin formation  
181 (Fig. 2d). These results suggested that cohesin loading accumulation is dependent on  
182 Rad21-loader interaction, and cohesin with LIS-mutant-Rad21 functions as an intact complex  
183 before loading onto chromatin. FRAP experiments further showed that the vermicelli pattern  
184 disappeared when LIS of Rad21 was deleted or replaced by poly-Ala in HeLa cells with  
185 Rad21-GFP over-expression (Fig. 2d and Supplementary information, Fig. S2c), while mutant  
186 LIS1 showed less modulation compared with LIS2 in FRAP assays (Fig. 2e, f).

187 To test whether SMC1A and SMC3-loader interaction dysfunction could disrupt  
188 Rad21-mediated cohesin loading, we constructed LIS poly-Ala mutants for SMC1A and  
189 SMC3, respectively (Supplementary information, Fig. S2d). In such conditions, the  
190 Rad21-vermicelli pattern persisted and colocalized with mutant SMC1A, but not mutant  
191 SMC3, which suggested that SMC1A interaction with the loader is dispensable for the  
192 cohesin loading process (Fig. 2g).

193 To quantify the cohesin loading capability of cohesin subunits, we applied single molecule  
194 tracking of Rad21, with H2A as a reference, in living HeLa cells. For single-molecule  
195 imaging, we used highly inclined illumination microscopy to reduce background noise. The  
196 data showed that the majority of cohesin subunit molecules were stationary and only a small  
197 fraction was mobile, suggesting that up-regulated Rad21 was prone to bound stably to  
198 chromatin (Supplementary information, Fig. S2e).

199

200 **Excessively loaded cohesin are anchored by CTCF and saddle on topologically**  
201 **associating domains**

202 Previous studies have suggested that cohesin complexes condense chromatin DNA by  
203 progressively extruding DNA with the help of NIPBL and MAU2<sup>23</sup>, meanwhile CTCF works  
204 as the boundary to halt the extrusion process resulting in the appearance of TADs. Notably,  
205 CTCF was enriched in vermicelli-like structures and colocalized with Rad21, which  
206 confirmed the association between CTCF and cohesin when extruding loops met their ends at  
207 CTCF sites (Fig. 3a, b). The distributions of NIPBL and MAU2 showed no significant  
208 difference between wild-type and RAD21-OE cells (Fig. 3a and Supplementary information,  
209 Fig. S3a), which was consistent with the dynamic motion of NIPBL during cohesin loading.  
210 We also calculated the co-localization ratio of CTCF and Rad21, and we found that CTCF  
211 was partially enriched in vermicelli-like structures, while most Rad21 was co-localized with  
212 CTCF (Fig. 3c), which corresponded with the ability of CTCF to function as a boundary  
213 element when chromatin over-extrusion occurs.

214 To visualize how TADs are organized in vermicelli-like structures, three TADs (*EMC7*  
215 chr7:5260000-5860000, *ACTB* chr7:5260000-5860000, *CD28* chr2:203600000-204400000)  
216 were labeled after Rad21 over-expression using fluorescence *in situ* hybridization (FISH)  
217 (Materials and Methods). The Rad21 “beads” were found to be localized at the middle of a  
218 TAD (Fig. 3d and Supplementary information, Fig. S3b). Interestingly, the normalized  
219 intensity profile of the boxed region measured across the center of the *EMC7* TAD and Rad21  
220 (n=20 per condition) detected that excessive cohesin saddled on TADs (Fig. 3e), which is

221 consistent with the CTCF/cohesin-anchored chromatin loop model<sup>4,7,8,12,19,24,27,28</sup> (Fig. 3f). We  
222 also calculated the volume of *EMC7* TAD and found that the median volume of TAD became  
223 larger in the presence of Rad21 up-regulation (Fig. 3g), suggesting that a larger range of  
224 intra-TAD interactions resulted from chromatin over-extrusion. Furthermore, we applied 1-hr  
225 EdU-Cy5 metabolic labeling<sup>29,30</sup> and found that the area of EdU clusters enlarged significantly  
226 after Rad21 was up-regulated (Supplementary information, Fig. S3c, d), which indicated  
227 overall enlargement of chromatin domains. To measure the 3D genome organizational change  
228 at a larger scale, we performed chromosome painting assays. Chromosome 2 was found to  
229 exhibit a fiber-like pattern in the presence of Rad21 over-expression (Fig. 3h, i), indicating  
230 that a global conformational effect within a single chromosome was conferred by over-loaded  
231 cohesin. We also found that the volume of chromosome 2 became slightly larger after Rad21  
232 over-expression during the formation of vermicelli-like structures (Supplementary  
233 information, Fig. S3e). Taken together, these data suggest that over-loaded cohesin could  
234 facilitate the formation of larger TADs through the processive extrusion of nearby small TADs  
235 and therefore affect macro-scale chromosome organization.

236

### 237 **Rad21 up-regulation affects genome contacts by stimulating cohesin activity**

238 To study the effect of Rad21 over-expression on genome organization, we performed Hi-C  
239 assays in HeLa cells in the presence and absence of Rad21 up-regulation to study the  
240 macro-scale consequences on chromosome architecture. The relative contact probability  
241 indicated that the genome-wide/global chromosomal contact frequency increased for short  
242 distance interactions (0.3–6 Mb) and decreased for long distance interactions (>6 Mb) in

243 Rad21-OE cells (Fig. 4a). For intra-chromosomal interactions, taking chromosome 2 as an  
244 example, Hi-C contact matrices showed that the number of far-cis contacts markedly  
245 decreased after Rad21 was up-regulated, whereas the number of short-distance contacts  
246 increased (Fig. 4b). The inter-chromosome interaction ratio was significantly decreased after  
247 Rad21 up-regulation (Supplementary information, Fig. S4a). These findings are in line with  
248 the notion that chromosome condensation and segregation occur with the formation of  
249 vermicelli-like structures in Rad21-OE cells.

250 We next explored the effect of Rad21 over-expression on nuclear compartmentalization,  
251 namely compartments A and B, which are defined by the first principal component (PC1) of  
252 Hi-C correlation matrices. In Rad21 up-regulated cells, we detected decreased intensity of  
253 “checkerboard” patterns, and the distribution of the PC1 scores was less strongly bimodal  
254 (Fig. 4c), suggesting a decrease in the compartmentalization level of chromosomes in  
255 Rad21-OE cells. To quantify the change of compartmentalization for each chromosome, we  
256 calculated the ratio of the interaction frequency between different classes of compartments  
257 (AB) versus that between the same classes of compartments (AA and BB)<sup>31</sup>. These ratios were  
258 significantly increased in Rad21-OE cells (Fig. 4d), indicating less strict segregation between  
259 the A and B compartments. We also calculated the average contact frequency enrichment of  
260 compartments ranked by PC1 values, which indicated increasing contact enrichment between  
261 different compartment categories and decreasing contact enrichment between similar  
262 compartment categories (Fig. 4e). Moreover, 1.9% of genomic regions switched from the A  
263 compartment to the B compartment after Rad21 was up-regulated, while 4.3% of genomic  
264 regions exhibited the opposite change (Fig. 4f).

265 We further applied an imaging approach to investigate the effect of Rad21 over-expression  
266 on chromatin structure. To visualize the effects of Rad21 over-expression on key epigenomic  
267 features associated with genome folding directly, we labeled two histone modifications,  
268 histone H3 lysine 4 trimethylation (H3K4me3) and histone H3 lysine 27 trimethylation  
269 (H3K27me3), which are associated with active and repressive chromatin in compartments A  
270 and B, respectively<sup>1,3,32</sup>. Rad21 over-expression had little effect on these features (Fig. 4g).  
271 Notably, the distribution of HP1 $\alpha$  was unchanged in the Rad21-OE cells, indicating that the  
272 formation of vermicelli-like structures was not dependent on heterochromatin (Fig. 4h).

273 To obtain a better understanding of the increase in the physical volume of TADs after  
274 Rad21 was up-regulated (Fig. 3g), we performed TAD calling on whole-genome contact maps  
275 and calculated TAD length. Notably, there was no significant change in TAD length after  
276 Rad21 was up-regulated (Supplementary information, Fig. S4b). In addition, no significant  
277 difference was observed in the number of long (>500 kb) or short (<500 kb) TADs  
278 (Supplementary information, Fig. S4c), and the insulation scores of TAD borders were similar  
279 (Supplementary information, Fig. S4d). These findings indicate that the insulation potential  
280 remained unchanged following up-regulation of Rad21. Therefore, over-loaded cohesin could  
281 lessen TADs and thus increase the accessibility of their associated chromatin.

282 To further probe how Rad21 over-expression regulates TAD structure, we visualized the  
283 interaction heat map at 40 kb resolution. After Rad21 was over-expressed, Hi-C contacts  
284 accumulated in TAD corners where CTCF binding sites are located (Fig. 4i). Aggregated TAD  
285 analysis (ATA) showed that this effect was global (Fig. 4j). Interestingly, the increase in the  
286 signal at the corners of TADs was accompanied by a decreased TAD score (contact frequency

287 ratio between intra-TADs and inter-TADs) (Fig. 4k). Taken together, our results suggest that  
288 over-loaded cohesin facilitates the formation of chromatin loops that span the maximal  
289 distance within TADs through processive extrusion, which led to increased inter-TAD contact  
290 frequency.

291

### 292 **Rad21 up-regulation is involved in breast cancer by affecting chromatin architecture**

293 Next, we explored the pathological relevance of genome structural disorders caused by Rad21  
294 up-regulation. We first studied clinical data from The Cancer Genome Atlas (TCGA).  
295 Through Kaplan-Meier survival analysis, we found that patients with higher Rad21  
296 expression levels did not survive as long as patients with low levels (Fig. 5a). In addition, the  
297 Rad21 expression levels in the breast cancer tissues of patients with four cancer subtypes  
298 were significantly higher than those measured in normal tissues (Fig. 5b). Moreover, several  
299 studies have found that enhanced Rad21 transcription is correlated with increased gene copy  
300 number in breast cancer tissue, which is associated with poor prognosis and resistance to  
301 chemotherapy<sup>33,34</sup>. Another study proposed that Rad21 could be a target for breast cancer  
302 drugs, because Rad21-targeted siRNA increased the sensitivity of cells to two  
303 chemotherapeutic drugs<sup>35</sup>. Therefore, we explored the relationship between genome  
304 organization disorders associated with enhanced Rad21 expression and breast cancer  
305 oncogenesis and prognosis.

306 To assess Rad21 aggregation in breast cancer cells with high Rad21 expression levels, we  
307 obtained three human breast cancer cell lines with high levels of Rad21 expression<sup>34,35</sup>, and  
308 the MCF10A cell line was used as a reference. The Rad21 level of each cell line was

309 measured by western blotting (Supplementary information, Fig. S5a). Super-resolution  
310 imaging was used to reveal the endogenous distribution of Rad21. Compared with MCF10A  
311 cells, Rad21 was more aggregated and showed a high level of heterogeneity in the three  
312 selected breast cancer cell lines, indicating a tendency for the formation of vermicelli-like  
313 structures (Fig. 5c, d and Supplementary information, Fig. S5b).

314 To explore the influence of Rad21 up-regulation, we analyzed gene expression in control  
315 and Rad21-OE cells. This analysis revealed 649 significantly up-regulated (fold change > 2,  
316 p-value < 0.05) and 138 down-regulated genes (fold change < 0.5, p-value < 0.05) in  
317 Rad21-OE cells (Fig. 5e and Supplementary information, S5c). The top 8 Kyoto  
318 Encyclopedia of Genes and Genomes (KEGG) pathways for differentially expressed genes  
319 were obtained (Supplementary information, Fig. S5d). Among the top 8 KEGG pathways,  
320 cytokine-cytokine receptor interaction, the TNF signaling pathway and the NOD-like receptor  
321 signaling pathway are known to play roles in breast cancer<sup>36-38</sup>. In addition, to obtain insight  
322 into the relationship between up-regulated Rad21 and breast cancer, we subjected breast  
323 cancer cell lines to gene set enrichment analysis (GSEA). The GSEA identified significant  
324 enrichment of mutant TP53, over-expressed KRAS and up-regulated EGFR target genes  
325 following Rad21 up-regulation (Supplementary information, Fig. S5e). These gene sets  
326 contain several genes that have been widely studied in the context of cancer, including  
327 *WNT16*, *CEBPD* and *EGFR*.

328 Additional analysis was performed to clarify the association between genome structural  
329 disorders caused by vermicelli-like structures and differential gene expression. We found that  
330 the compartment switch from B to A coincided with higher expression levels, while the switch

331 from compartment A to B was not associated with a significant change (Fig. 5f). One of the  
332 up-regulated genes in the compartment B-to-A switch region was cell migration inducing  
333 hyaluronidase 1 (*CEMIP*), which has been reported to promote the proliferation and migration  
334 of breast cancer cells<sup>39,40</sup>. A high CEMIP protein expression level is significantly associated  
335 with poor patient survival<sup>41</sup>. These results suggest that compartment switching as a result of  
336 Rad21 up-regulation can lead to up-regulation of cancer-related genes.

337 In addition, TAD insulation was also correlated with gene expression. We calculated the  
338 TAD score within differentially and stably expressed genes, revealing that both up-regulated  
339 and down-regulated genes had reduced TAD score. These results indicated that stronger  
340 inter-TAD interactions could affect the expression of genes within the interacting domains  
341 (Fig. 5g). These results revealed the connection between breast cancer and genome structural  
342 changes upon Rad21 up-regulation.

343

## 344 **Discussion**

345 Here, we provide key insights into the molecular mechanism by which Rad21 facilitates the  
346 cohesin loading process and thus directing genome organization using live cell  
347 super-resolution imaging and biochemical approaches. We observed that excess Rad21 led to  
348 intensive chromatin condensation and vermicelli-like distribution of cohesin. Importantly, we  
349 revealed that this process was driven by enhanced loading of the cohesin complex, while the  
350 amount of unloaded cohesin was unaffected. These results suggest that Rad21 acts as a crucial  
351 factor in cohesin loading. Mechanistically, Rad21 mutants that are unable to bind the cohesin  
352 loader complex cannot lead to the vermicelli-like pattern, indicating that Rad21-loader

353 interaction is an important determinant in the cohesin loading process. After Rad21  
354 up-regulation, accumulated contacts were shown at TAD corners and inter-TAD interactions  
355 increased. At the subchromosome scale, chromatin interactions between A and B  
356 compartments increased and compartmentalization strength was reduced significantly (Fig.  
357 6).

358 According to previous studies, cohesin was found to form a thread-like distribution that has  
359 been described as “vermicelli-like”, and chromatin condensation was shown to be enhanced  
360 in mouse embryonic fibroblasts (MEFs) after cohesin was stabilized on chromatin by Wapl  
361 depletion. In contrast, our findings showed that over-expression of cohesin subunit Rad21 led  
362 to accumulation of cohesin on chromatin and a vermicelli thread-like cohesin distribution in  
363 the nucleus of human HeLa cells, while cohesin release from chromatin mediated by Wapl  
364 remained unchanged. We therefore inferred that Rad21 is an important factor that affects  
365 cohesin loading independent of Wapl.

366 Previous studies have established that the loader complex SCC2/SCC4 is essential for  
367 cohesin loading onto chromatin<sup>17,42-44</sup>. In addition, Murayama and Uhlmann showed that  
368 Rad21 interacts directly with the loader complex in *S. pombe* using tiling peptide arrays<sup>22</sup>. *In*  
369 *vitro* translated Scc1 was found to bind GST-Scc2, and the binding region of Scc1 was  
370 mapped to residues 126–230<sup>45</sup>. The different impact of the LIS mutant of each cohesin  
371 subunit suggests that Rad21-LIS is crucial for cohesin loading on DNA and further activation.  
372 A recent cryo-EM study of the human cohesin-NIPBL-DNA complex shed new light on the  
373 structural details of Rad21-loader interactions<sup>24</sup>. The cohesin-NIPBL-DNA complex consists  
374 of the V-shaped SMC1-SMC3 heterodimer, the U-shaped NIPBL and the SMC1-SMC3 hinge

375 domains with or without SA1. The complex is stabilized by DNA bound at the central tunnel  
376 and surrounding flexible Rad21. The LIS of cohesin is missing from the structure with the  
377 exception of LIS2 of Rad21, which mediates Rad21-MAU2 interaction. Rad21 LIS2 is bound  
378 by U-shaped SA1 and is located close to the DNA binding interface of SA1, while the missing  
379 Rad21 LIS1 is close to the external surface of the NIPBL HEAT repeat (R6, R7, R10), which  
380 directly interacts with DNA via its internal surface. Our colocalization results (Supplementary  
381 information, Fig. S1d) indicate that SA1 is not a constitutive component of cohesin, in line  
382 with poorly resolved cryo-EM results, which may due to its low binding occupancy.

383 In addition, Rad21-loader specific interaction may be important in cohesin regulation. For  
384 example, recombinant *Chaetomium thermophilum* (Ct) Pds5 competes with Ct Scc2 for  
385 binding to Scc1 *in vitro* in a dose-dependent manner, indicating that it possesses the ability to  
386 release Scc2 for the next round of cohesin loading<sup>45</sup>. It was also reported that most (16 of 19)  
387 Ct Scc2 mutants were deficient in binding to the N-terminal of Ct Scc1 in patients with the  
388 human developmental disorder termed Cornelia de Lange syndrome (CdLS)<sup>45</sup>. Considering  
389 our findings, it is possible that Scc2 mutants impair cohesin loading and disrupt  
390 enhancer-promoter chromatin loop formation at genes with important functions in  
391 development.

392 It is widely accepted that CTCF and cohesin work as boundary elements for chromatin loop  
393 extrusion based on the observations that many CTCF binding sites are enriched in the bases of  
394 chromatin loop domains in GM12878 cells<sup>3</sup> and the boundary regions of TADs in IMR90  
395 cells<sup>2</sup>. The association of CTCF and cohesin clusters was demonstrated by two-color direct  
396 stochastic optical reconstruction microscopy (dSTORM) super-resolution imaging in mES

397 cells, in which these clusters overlap were found to largely overlap<sup>46</sup>. Consistent with this  
398 study, our results showed colocalization of CTCF and cohesin in the presence of  
399 vermicelli-like patterns. Furthermore, cohesin was found to be essential for the formation and  
400 maintenance of TADs and loops. For example, the loop domains disappeared after cohesin  
401 was depleted by auxin, and most loop domains recovered in 1 h after auxin was withdrawn in  
402 the auxin-inducible degron HCT-116 cell line<sup>4</sup>. Remarkably, Both TADs and loops were  
403 greatly reduced after 180 min of auxin treatment in Scc1-mEGFP-AID HeLa cells<sup>27</sup>. Our  
404 results showed the distribution of cohesin and TADs directly in the nucleus for the first time.  
405 We found that cohesin complexes were enriched in the bases of TADs, which was consistent  
406 with the hypothesized model that multiple loop-extrusion cohesin complexes extrude longer  
407 chromatin loops constantly within the TAD, the complexes were halted by CTCF binding in a  
408 convergent direction at the boundary region of TADs<sup>47</sup>. Longer loops also led to stronger  
409 inter-TAD interactions after Rad21 up-regulation.

410 A previous chromosome spreading study using yeast revealed the presence of 100 or more  
411 Scc1 foci<sup>48</sup>. In another study, quantitative western blotting revealed 5–20 cohesin complexes  
412 at each cohesin binding site, indicating that cohesin may associate with chromatin in clusters<sup>49</sup>.  
413 Similarly, 5–15 cohesin molecules were found in cohesin clusters in mES cells by live cell  
414 STED imaging<sup>50</sup>. Recently, a new type of phase separation mediated by the SMC protein of  
415 the cohesin complex, termed bridging-induced phase separation (BIPS), was reported in a  
416 study that showed formation of cohesin-DNA clusters after the application of 10 nM yeast  
417 cohesin holocomplexes to double-tethered  $\lambda$ DNA. Following the application of cohesin  
418 holocomplexes, cluster fusion and rapid recovery after photobleaching were observed, which

419 suggested liquid-like behavior<sup>50</sup>. Consistent with the studies described above, we observed the  
420 formation of bead-like clusters in living cells following Rad21 over-expression, and these  
421 clusters were located close to TADs labeled by FISH. It is possible that the accumulated  
422 cohesin complexes at the boundary regions of TADs mediate the formation and maintenance  
423 of chromatin loop domains in the interphase by self-association. However, whether the  
424 distribution of cohesin complexes at TAD boundaries is liquid-like cluster or vermicelli-like  
425 under physiological conditions is unknown.

426 Somatic mutations and amplification of Rad21 have been widely reported in both human  
427 solid and hematopoietic tumors. Rad21 alterations are relatively common according to TCGA  
428 PanCancer atlas studies (7% of all queried patients), which show elevated Rad21 in 20% of  
429 ovarian cancer cases and 13% of breast cancer cases. Over-expression of Rad21 has been  
430 linked with epithelial breast cancer and has been found to be correlated with poor disease  
431 outcome and resistance to chemotherapy. Although the correlation between Rad21 expression  
432 and cancer risk is relatively well established, little is known regarding the causes and  
433 consequences of Rad21 over-expression in tumorigenesis. In our study, we monitored the  
434 outcomes of Rad21 over-expression in HeLa cells and compared the effects of elevated Rad21  
435 on gene expression with TCGA BRCA studies. Unfortunately, we were unable to generate a  
436 stable Rad21 over-expression cell line, perhaps due to activation of the TNF- $\alpha$  apoptosis  
437 signaling pathway. By comparing transcriptome changes and chromatin structure alterations  
438 upon Rad21 up-regulation, we demonstrated that the relationship between Rad21  
439 up-regulation and breast cancer is likely mediated by changes in chromatin architecture, and  
440 we found that chromatin alterations and transcriptional changes following Rad-21

441 up-regulation were consistent. Taken together, our findings suggest that Rad21 plays a key  
442 role in regulating chromatin structure and acts as an oncogene. This study provides important  
443 information describing the relationship between chromatin status and the etiology of cancers,  
444 which may reveal new targets for clinic treatments.

445

## 446 **Materials and methods**

### 447 **Cell Culture**

448 The human HeLa-S3 immortalized cell line (Catalog No. 30-2004) and human SK-BR-3 cell  
449 line (Catalog No. 30-2007) were grown at 37 °C with 5% CO<sub>2</sub> in high-glucose DMEM  
450 (Thermo Scientific, 11965084) containing 10% (v/v) fetal bovine serum (HyClone,  
451 SV30087.02) and 100 U/mL Penicillin Streptomycin (Thermo Scientific,15140163). The  
452 human MCF10A cell line (Catalog No. CC-3150) was grown at 37 °C with 5% CO<sub>2</sub> in  
453 MEGM Mammary Epithelial Cell Growth Medium (Lonza, CC-3150) containing  
454 supplements required for growth. The human MDA-MB-157 cell line (Catalog No. 30-2008)  
455 was grown at 37 °C without CO<sub>2</sub> equilibration in Leibovitz's L-15 Medium (Thermo  
456 Scientific, 11415-064) supplemented with 10% (v/v) fetal bovine serum and 100 U/mL  
457 Penicillin Streptomycin. The human HCC1395 cell line was cultured in RPMI 1640 Medium  
458 (Thermo Scientific,11875093) containing 10% (v/v) fetal bovine serum and 100 U/mL  
459 Penicillin Streptomycin at 37 °C with 5% CO<sub>2</sub>.

460 **Live cell imaging and analysis**

461 The Human SMC1A, SMC3, Rad21, and SA1/2 genes were tagged with Halo tag or EGFP  
462 and cloned into the pcDNA3.1 vector by Gibson assembly. Cells were plated in glass-bottom  
463 dishes, transfected with 2  $\mu$ g of the indicated plasmids, and allowed to grow for 24–36 h.  
464 Cells were then labelled with 1  $\mu$ M JF549 (Promega, 6147/5) for more than 15 min and rinsed  
465 twice with PBS before imaging. The dishes were then incubated at 37 °C with 5% CO<sub>2</sub> in the  
466 incubation chamber of the microscope. Super resolution live-cell imaging was performed  
467 using a spinning disk confocal system (Nikon, live SR CSU W) with an EMCCD (iXon  
468 DU-897E) mounted on a Nikon Ti-E microscope with a CFI Apo TIRF 100  $\times$  Oil (N.A. 1.49)  
469 objective.

470 For FRAP assays, the cells were transfected with 2  $\mu$ g of plasmids containing a gene  
471 labelled by an EGFP tag for 24–36 h. One pre-bleach image was acquired, after which one  
472 half of a nucleus was bleached with the 488 nm laser (100% laser power), and recovery  
473 images were acquired by a confocal microscope (Carl ZEISS, LSM880).

474 For single molecule imaging assay, cells were labelled with 0.1 nM JF549 for more than 15  
475 min and rinsed twice with PBS before imaging. In order to collect a sparse single molecule  
476 signal, cells were photo-bleached with a strong laser. The time-lapse imaging data was  
477 acquired on a custom-built microscope (Olympus, IX83) with a 10 ms exposure time.

478 The single-molecule signal was recognized and tracked using the FIJI (Fiji Is Just ImageJ)  
479 plugin for Trackmate software. The diffusion coefficient was then obtained as previously  
480 described<sup>51</sup> using the following formula:

481

$$\text{diffusion coefficient} = \frac{\Delta x^2 + \Delta y^2}{4 * \Delta t}$$

482

483 where  $\Delta x$  and  $\Delta y$  represent the step size during the time interval  $\Delta t$ .

484 The distribution of the diffusion coefficient value was fitted with a Gaussian function using

485 Origin software.

#### 486 **Immunofluorescence**

487 Cells were fixed using 4% (w/v) paraformaldehyde (Electron Microscopy Sciences, 157-8) in

488 PBS (Thermo Scientific, 14190144) for 15 min, followed by three washes in PBS.

489 Permeabilization of cells was performed using 0.5% Triton X-100 (Sigma-Aldrich, T8787-50

490 ML) in PBS for 10 min, followed by blocking with 5% IgG-free bovine serum albumin (BSA,

491 Jackson, 001-000-162) for 30 min. The indicated primary antibody was added to 5% BSA in

492 PBS at an appropriate dilution and incubated overnight at 4 °C. After 3 rinses in PBS, cells

493 were incubated with a secondary antibody labeled with an Alexa Fluor dye at a dilution of

494 1:200 in PBS with 5% BSA for 1 h. The cells were then rinsed with PBS 3 times and fixed

495 using 4% PFA in PBS for 10 min. After 2 rinses in PBS, the cells were finally stored in PBS.

496 Imaging data were acquired using a spinning disk confocal system (Nikon, live SR CSU W1)

497 with an EMCCD (iXon DU-897E) mounted on a Nikon Ti-E microscope with a CFI Apo

498 TIRF 100 × Oil (N.A. 1.49) objective.

499 For STED (Leica, TCS SP8 STED 3X) imaging, the sample preparation method was

500 identical to the procedure described above, except that the secondary antibody was a donkey

501 anti-Rabbit IgG secondary antibody (Alexa Fluor 594).

<b>ANTIBODY</b>	<b>IDENTIFIER</b>	<b>SOURCE</b>
Anti-Histone H2B	ab1790	abcam
Anti-Histone H3	ab1791	abcam
Anti-Histone H3 (tri methyl K4)	ab8580	abcam
Anti-Histone H3 (tri methyl K27)	ab6002	abcam
Anti-CTCF	ab128873	abcam
Anti-SMC1A	ab133643	abcam
Anti-SMC3	ab9263	abcam
Anti-SA1	ab4455	abcam
Anti-NIPBL	ab220952	abcam
Anti-Scc4	ab183033	abcam

<b>ANTIBODY</b>	<b>IDENTIFIER</b>	<b>SOURCE</b>
Donkey anti-Rabbit IgG (H+L) Secondary Antibody,	A-21206	Thermo Scientific

---

Alexa Fluor 488

Donkey anti-Mouse IgG

A-21202

Thermo Scientific

(H+L) Highly

Cross-Adsorbed Secondary

Antibody, Alexa Fluor 488

Donkey anti-Rabbit IgG

A-21207

Thermo Scientific

(H+L) Highly

Cross-Adsorbed Secondary

Antibody, Alexa Fluor 594

Donkey anti-Mouse IgG

R37115

Thermo Scientific

(H+L) ReadyProbes&trade;

Secondary Antibody, Alexa

Fluor 594

---

504

505 **Heterogeneity level analysis**

506 The nucleoli and extranuclear regions were manually selected from the image and the

507 intensity (gray value) of these parts was set to 0. The average intensity of each image was set

508 to the same value to eliminate cell heterogeneity. Considering the radial distance of the

509 vermicelli-like structures was approximately 5 pixels, we used a 5 × 5-pixel box traversing

510 the image and calculated the intensity of the box. If the intensity was 0, we discarded the

511 value, which represented the nucleoli or extranuclear region. To quantify the intensity of

512 different samples, we fitted the distribution of intensity values with a double Gaussian  
513 function. The two Gaussian peaks represented the distributions of the sparse regions and  
514 dense regions respectively. The heterogeneity level was acquired by calculating the distance  
515 between the two peaks. A custom-written MATLAB program was used for the analysis.

#### 516 **Co-immunoprecipitation (co-IP) assay**

517 GFP-positive HeLa cells transfected with the indicated plasmids were collected using FACS  
518 (BeckMan Coulter, Astrios EQ). Generally,  $10^6$  cells were sorted, washed twice with PBS,  
519 and lysed in a buffer containing 20 mM Tris-HCl (pH 7.5), 100 mM NaCl, 5 mM EDTA, 1%  
520 Triton X-100, 0.5% NP-40, 0.1% SDS and protease inhibitors. After incubation at 4 °C for 10  
521 min, the soluble fraction (containing 0.1 M NaCl) was separated from the chromatin fraction  
522 by centrifugation at  $15,000 \times g$  for 10 min. The chromatin pellet was then incubated in the  
523 above buffer with the addition of 0.5 M NaCl at 4 °C for 1 h, followed by centrifugation at  
524  $15,000 \times g$  for 10 min. The final pellet was resuspended in 1 M NaCl of the above buffer,  
525 sonicated for 20 s (1 s on and 1 s off), incubated at 4 °C for 1 h, and then centrifuged. These  
526 lysate fractions were subjected to Co-IP with an antibody against SMC3 (abcam, ab9263).  
527 Further immunoblot analyses were performed with the following antibodies: H3 (Ruiying  
528 Biological Technology, RLM-3038), ACTB (ABclonal, AC026), Rad21 (Thermo Scientific,  
529 PA5-54128), and SMC3 (abcam, ab9263).

#### 530 **Chromosome painting**

531 Cells were plated on a coverslip, transfected with 2  $\mu$ g of the indicated plasmids, and allowed

532 to grow for 24 h. After fixation in 3:1 (v/v) methanol/acetic-acid, the cells were washed 3  
533 times in PBS. Cell permeabilization was performed using 0.5% Triton X-100 (Sigma-Aldrich,  
534 T8787-50 ML) in PBS for 10 min. Next, 10  $\mu$ L of a commercial probe mixture was applied  
535 (Sigma-Aldrich, D-0302-100-FI XCP 2), and the slide was sealed with rubber cement. The  
536 cells and probe were denatured by heating the slide on a hotplate at 75 °C for 2 min, followed  
537 by hybridization in a humidified chamber at 37 °C overnight. The slide was then removed  
538 from the chamber, and the coverslip was washed in 0.4 $\times$  SSC (Sigma-Aldrich, S6639-1L)  
539 (pH=7.0) at 72 °C for 2 min. The coverslip was dried, washed in 2 $\times$  SSC with 0.05%  
540 Tween-20 (Solarbio, T8220) (pH=7.0) at room temperature for 30 seconds, rinsed briefly in  
541 distilled water, and allowed to air-dry. Next, 10  $\mu$ L DAPI was applied to a clean slide and  
542 covered with the coverslip, followed by sealing with rubber cement. The slide was imaged  
543 with a confocal microscope (Nikon, Live SR CSU W1) with a 100 $\times$  objective. The imaging  
544 data were then processed using Fiji Is Just ImageJ (FIJI).

#### 545 **Probe design and construction**

546 Probe design and construction were performed with previously described methods<sup>30,52</sup>. In  
547 brief, oligonucleotide probes targeting specific genomic regions were designed following  
548 online instructions and the methods of Oligominer  
549 (<https://github.com/brianbeliveau/Oligominer>). The probes were amplified from complex  
550 oligonucleotide pools (Hongxun Biotech) by limited cycles of amplification. The templates in  
551 the oligonucleotide pools were designed to contain a 32-mer targeting region that is  
552 complementary to the genomic sequence, a 30-mer flanking sequence to be hybridized by the

553 secondary probes, as well as two 20-mer primer binding sequences to amplify the probes.

554 For probe construction, we firstly amplified the oligonucleotide pools via 26 cycles of PCR  
555 to generate templates for *in vitro* transcription (Phanta Max Super-Fidelity DNA Polymerase,  
556 #P505-d2). The PCR product was column-purified (Zymo DNA Clean and Concentrator,  
557 DCC-5) and then converted into RNA via *in vitro* transcription (HiScribe™ T7 High Yield  
558 RNA Synthesis Kit NEB, #E2040S). RNA templates were converted back to DNA via reverse  
559 transcription (MAN0012047 TS Maxima H Minus Reverse Transcriptase, Thermo Fisher  
560 #EP0751), and the single-stranded DNA products were then purified by alkaline hydrolysis  
561 (50 µL of 0.25 M EDTA and 0.5 M NaOH) and column purification (Zymo Research,  
562 #D4006). The concentrations of the composites were described in a previous work from our  
563 laboratory.

#### 564 **Fluorescence *in situ* hybridization**

565 For FISH experiments, the cell sample preparation methods were identical to those used for  
566 the immunofluorescence experiments. After fixation using 4% (w/v) paraformaldehyde for 15  
567 minutes, the samples were incubated in 1x PBST (1xPBS +1% (v/v) Triton X-100) for 10  
568 minutes and then rinsed twice with 1x PBST. Each sample was then incubated in 100 µg/mL  
569 RNaseA (TransGen Biotech, GE101-01) to remove RNA followed by incubation in 0.1M HCl  
570 in 1x PBST for 10 minutes, washed 3 times in 1x PBST, washed 3 times in 2x SSCT (2x  
571 saline sodium citrate + 1% (v/v) Triton X-100) at RT, and incubated in 2x SSCT + 50% (v/v)  
572 formamide at 4 °C overnight. For sample prehybridization, the samples were incubated in 50%  
573 formamide (Sigma-Aldrich, 47671) + 2x SSCT at 78 °C for 10 minutes and then dehydrated

574 by incubation in 70%, 85%, and 100% ice-cold ethanol successively, for 1 min each. For  
575 probe prehybridization, synthesized primary probes (5  $\mu$ L) and secondary probes (1 $\mu$ L, 100  
576  $\mu$ M) were mixed with 100% formamide (35  $\mu$ L), after which the probe mixture was incubated  
577 in a mixer for 15 min at 37 °C. Next, pre-warmed 20% (w/v) dextran (Sigma-Aldrich,  
578 D8906-10G) (35  $\mu$ L) was added to the mixture, which was incubated in a mixer for 30 min at  
579 37 °C. Finally, the mixture was incubated at 86 °C for 3 minutes and cooled on ice  
580 immediately.

581 Samples were then denatured for 3 minutes at 86 °C and hybridized at 37 °C in a  
582 humidified chamber overnight. The hybridized samples were then rinsed twice for 15 minutes  
583 in pre-warmed 2x SCCT at 60 °C, followed by washing for 10 minutes in 2x SSC at room  
584 temperature, and stored at 4 °C in 2x SSC before imaging.

#### 585 **Cell synchronization and nucleotide labelling**

586 Cells were grown on glass-bottom dishes and synchronized at the G1/S transition by 2 mM  
587 thymidine (Sigma-Aldrich, T1895) for 15 h, followed by culturing in fresh DMEM for 10 h,  
588 and treatment with 2  $\mu$ g/mL aphidicolin (abcam, ab142400) for 15 h.

589 To incorporate EdU in HeLa cells, the cells were bathed with growing medium containing  
590 EdU for 30 min after releasing them from the G1/S transition for 1 h, followed by growth in  
591 fresh DMEM for 2 days. The cy5 dye was then conjugated to EdU using the Click-iT EdU  
592 Imaging Kit (Thermo Scientific, C10340) according to the manufacturer's instructions.  
593 Imaging data were acquired using the spinning disk confocal system described above.

594 **Radius of gyration analysis**

595 3D chromosome morphology was first segmented from 3D images using the Imaris Volume  
596 module with its default parameters, after which we labeled each 3D chromosome according to  
597 its connectivity and obtained the coordinates and intensity (gray value) of each voxel within  
598 each chromosome using custom-written MATLAB scripts. The radius of gyration (R<sub>g</sub>) was  
599 obtained as the following formula:

$$R_g = \sqrt{\frac{\sum_i I_i (\vec{r}_i - \vec{r}_c)^2}{\sum_i I_i}}$$

600 where  $\vec{r}_c$  is the center,  $\vec{r}_i$  and  $I_i$  are the position and intensity of the  $i$ -th voxel.

601 **Cluster size analysis**

602 Clusters were recognized using the Surfaces module including with the Imaris software  
603 package. The “diameter of largest sphere” was set to 0.492 μm, the threshold value was set to  
604 25, and the remaining parameters were set to their default values. When the search was  
605 complete, we then erased the signal outside the nuclei manually. Finally, the area and other  
606 cluster properties were exported by Imaris automatically for the subsequent statistical  
607 analysis.

608 **In situ Hi-C**

609 The *in situ* Hi-C libraries was generated as previously described (Rao et al., 2014). Briefly,  
610 cells were grown to approximately 70–80% confluence, washed with PBS, fixed in 1%  
611 formaldehyde, and suspended in Hi-C lysis buffer to which 100 U MobI restriction enzyme

612 (NEB, R0147) was added for overnight chromatin digestion. Free ends were labeled with  
613 biotin and then ligated together *in situ*. Crosslinks were reversed, the DNA was sheared to  
614 produce 300–500 bp fragments, and then biotinylated ligation junctions were recovered with  
615 streptavidin beads. Hi-C libraries were amplified using PCR, constructed according to the  
616 NEBnext library preparation protocol (NEB, E7335), and sequenced on the Illumina HiSeq X  
617 Ten platform.

### 618 **Hi-C data analysis**

619 Hi-C data were processed by HiC-Pro<sup>53</sup>. Briefly, reads were first aligned on the hg19  
620 reference genome. Uniquely mapped reads were normalized using Iterative Correction and  
621 Eigenvector (ICE) decomposition and library size. For compartment A/B analysis, HiTC<sup>54</sup>  
622 was used to visualize the interaction matrix and calculate the PC1 (at 150-kb resolution).  
623 Compartment switches were defined by comparing the PC1 values between Rad-OE cells and  
624 control cells, using zero as the PC1 cutoff. For TAD analysis, ICE-normalized 40-kb  
625 resolution matrices were used to detect TAD with a script described by Crane et al  
626 (<https://github.com/dekkerlab/crane-nature-2015>). Insulation scores were calculated for each  
627 40-kb bin, and the valleys of the insulation score curves were defined as TAD boundaries<sup>55</sup>.  
628 CTCF annotation was generated by GENOVA<sup>56</sup>. Aggregate TAD analysis was performed  
629 using cooltools (v0.4.0)<sup>57</sup>.

### 630 **RNA-seq experiments**

631 Total RNA was extracted using the MolPure Cell RNA Kit (YEASEN, 19231ES50). RNA

632 sequencing libraries were constructed using the NEBNext Ultra RNA Library Prep Kit for  
633 Illumina® (NEB England BioLabs). RNA-seq paired-end reads were sequenced on the  
634 Illumina NovaSeq 6000 platform.

### 635 **RNA-seq data analysis**

636 The raw RNA sequences were cleaned using TrimGalore  
637 ([https://www.bioinformatics.babraham.ac.uk/projects/trim\\_galore/](https://www.bioinformatics.babraham.ac.uk/projects/trim_galore/)) and mapped to human  
638 reference genome hg19 by STAR (v2.7.1a) with default parameters. All mapped bam files  
639 were converted to bigwig using bedtools (v2.24.0)<sup>58</sup>. for visualization in IGV. High-quality  
640 mapped reads were quantified using htseq-count (v0.11.3)<sup>59</sup>. Differentially expressed genes  
641 were analyzed by DEseq2<sup>60</sup>. Functional enrichment of previously reported gene sets in the  
642 transcriptomes between Rad21-OE and control cells was determined using the GSEA  
643 software package<sup>61,62</sup>. GO enrichment analysis was performed using Enrichr<sup>63</sup>.

644

### 645 **Data availability**

646 All Hi-C and RNA-seq datasets have been deposited in GEO under the accession number  
647 GSE183186.

648

### 649 **Acknowledgements**

650 We thank Dr. Wei Guo from University of Pennsylvania for providing HeLa-S3 cell line. We  
651 also thank Dr. Chunyan Shan from Core Facilities at School of Life Sciences, Peking  
652 University for assistance with super-resolution imaging. We thank the flow cytometry Core at

653 National Center for Protein Sciences at Peking University, particularly Dr. Hongxia Lv,  
654 Liying Du and Jia Luo, for technical help. This work is supported by grants from This work is  
655 supported by grants from the National Key R&D Program of China for Y.S. (No.  
656 2017YFA0505300) and the National Science Foundation of China for Y.S. (21825401).

657

#### 658 **Author Contributions**

659 Y.S. and Y.A.S. conceived of the study. Y.S. supervised the study. Y.S., Y.A.S., X.X., and  
660 W.X.Z. designed the experiments. Y.A.S. conducted all imaging experiments with help from  
661 K.Y.C, X.T.W. X.X. performed co-IP and western blotting experiments. W.X.Z. performed  
662 bioinformatics analysis. Y.Z. prepared the Hi-C library. Y.Z.L, and M.L.Z. designed and  
663 constructed the probe. Y. Hou contributed technical assistance/suggestions. Y.S., Y.A.S., X.X.,  
664 and W.X.Z wrote the manuscript with input from all authors.

665

#### 666 **Conflict of Interest**

667 The authors declare no competing financial interests.

668

#### 669 **References**

- 670 1 Lieberman-Aiden, E. *et al.* Comprehensive mapping of long-range interactions  
671 reveals folding principles of the human genome. *Science* **326**, 289-293,  
672 doi:10.1126/science.1181369 (2009).
- 673 2 Dixon, J. R. *et al.* Topological domains in mammalian genomes identified by analysis  
674 of chromatin interactions. *Nature* **485**, 376-380, doi:10.1038/nature11082 (2012).

- 675 3 Rao, S. S. *et al.* A 3D map of the human genome at kilobase resolution reveals  
676 principles of chromatin looping. *Cell* **159**, 1665-1680, doi:10.1016/j.cell.2014.11.021  
677 (2014).
- 678 4 Rao, S. S. P. *et al.* Cohesin Loss Eliminates All Loop Domains. *Cell* **171**, 305-320  
679 e324, doi:10.1016/j.cell.2017.09.026 (2017).
- 680 5 Vietri Rudan, M. & Hadjur, S. Genetic Tailors: CTCF and Cohesin Shape the  
681 Genome During Evolution. *Trends Genet* **31**, 651-660, doi:10.1016/j.tig.2015.09.004  
682 (2015).
- 683 6 Nora, E. P. *et al.* Targeted Degradation of CTCF Decouples Local Insulation of  
684 Chromosome Domains from Genomic Compartmentalization. *Cell* **169**, 930-944  
685 e922, doi:10.1016/j.cell.2017.05.004 (2017).
- 686 7 Alipour, E. & Marko, J. F. Self-organization of domain structures by  
687 DNA-loop-extruding enzymes. *Nucleic Acids Res* **40**, 11202-11212,  
688 doi:10.1093/nar/gks925 (2012).
- 689 8 Fudenberg, G. *et al.* Formation of Chromosomal Domains by Loop Extrusion. *Cell*  
690 *Rep* **15**, 2038-2049, doi:10.1016/j.celrep.2016.04.085 (2016).
- 691 9 Nasmyth, K. Disseminating the genome: joining, resolving, and separating sister  
692 chromatids during mitosis and meiosis. *Annu Rev Genet* **35**, 673-745,  
693 doi:10.1146/annurev.genet.35.102401.091334 (2001).
- 694 10 Ganji, M. *et al.* Real-time imaging of DNA loop extrusion by condensin. *Science* **360**,  
695 102-105, doi:10.1126/science.aar7831 (2018).
- 696 11 Davidson, I. F. *et al.* DNA loop extrusion by human cohesin. *Science* **366**, 1338-1345,

697 doi:10.1126/science.aaz3418 (2019).

698 12 Kim, Y., Shi, Z., Zhang, H., Finkelstein, I. J. & Yu, H. Human cohesin compacts DNA  
699 by loop extrusion. *Science* **366**, 1345-1349, doi:10.1126/science.aaz4475 (2019).

700 13 Gruber, S., Haering, C. H. & Nasmyth, K. Chromosomal cohesin forms a ring. *Cell*  
701 **112**, 765-777 (2003).

702 14 Haering, C. H., Lowe, J., Hochwagen, A. & Nasmyth, K. Molecular architecture of  
703 SMC proteins and the yeast cohesin complex. *Mol Cell* **9**, 773-788 (2002).

704 15 Kueng, S. *et al.* Wapl controls the dynamic association of cohesin with chromatin.  
705 *Cell* **127**, 955-967, doi:10.1016/j.cell.2006.09.040 (2006).

706 16 Gandhi, R., Gillespie, P. J. & Hirano, T. Human Wapl is a cohesin-binding protein  
707 that promotes sister-chromatid resolution in mitotic prophase. *Curr Biol* **16**,  
708 2406-2417, doi:10.1016/j.cub.2006.10.061 (2006).

709 17 Ciosk, R. *et al.* Cohesin's binding to chromosomes depends on a separate complex  
710 consisting of Scc2 and Scc4 proteins. *Mol Cell* **5**, 243-254,  
711 doi:10.1016/s1097-2765(00)80420-7 (2000).

712 18 Tedeschi, A. *et al.* Wapl is an essential regulator of chromatin structure and  
713 chromosome segregation. *Nature* **501**, 564-568, doi:10.1038/nature12471 (2013).

714 19 Haarhuis, J. H. I. *et al.* The Cohesin Release Factor WAPL Restricts Chromatin Loop  
715 Extension. *Cell* **169**, 693-707 e614, doi:10.1016/j.cell.2017.04.013 (2017).

716 20 Panizza, S., Tanaka, T., Hochwagen, A., Eisenhaber, F. & Nasmyth, K. Pds5  
717 cooperates with cohesin in maintaining sister chromatid cohesion. *Curr Biol* **10**,  
718 1557-1564, doi:10.1016/s0960-9822(00)00854-x (2000).

- 719 21 Chao, W. C. *et al.* Structural Studies Reveal the Functional Modularity of the  
720 Scc2-Scc4 Cohesin Loader. *Cell Rep* **12**, 719-725, doi:10.1016/j.celrep.2015.06.071  
721 (2015).
- 722 22 Murayama, Y. & Uhlmann, F. Biochemical reconstitution of topological DNA binding  
723 by the cohesin ring. *Nature* **505**, 367-371, doi:10.1038/nature12867 (2014).
- 724 23 Rhodes, J., Mazza, D., Nasmyth, K. & Uphoff, S. Scc2/Nipbl hops between  
725 chromosomal cohesin rings after loading. *Elife* **6**, doi:10.7554/eLife.30000 (2017).
- 726 24 Shi, Z., Gao, H., Bai, X. C. & Yu, H. Cryo-EM structure of the human  
727 cohesin-NIPBL-DNA complex. *Science* **368**, 1454-1459,  
728 doi:10.1126/science.abb0981 (2020).
- 729 25 Haering, C. H. *et al.* Structure and stability of cohesin's Smc1-kleisin interaction. *Mol*  
730 *Cell* **15**, 951-964, doi:10.1016/j.molcel.2004.08.030 (2004).
- 731 26 Higashi, T. L. *et al.* A Structure-Based Mechanism for DNA Entry into the Cohesin  
732 Ring. *Mol Cell* **79**, 917-933 e919, doi:10.1016/j.molcel.2020.07.013 (2020).
- 733 27 Wutz, G. *et al.* Topologically associating domains and chromatin loops depend on  
734 cohesin and are regulated by CTCF, WAPL, and PDS5 proteins. *EMBO J* **36**,  
735 3573-3599, doi:10.15252/emj.201798004 (2017).
- 736 28 Schwarzer, W. *et al.* Two independent modes of chromatin organization revealed by  
737 cohesin removal. *Nature* **551**, 51-56, doi:10.1038/nature24281 (2017).
- 738 29 Su, Q. P. *et al.* Superresolution imaging reveals spatiotemporal propagation of human  
739 replication foci mediated by CTCF-organized chromatin structures. *Proc Natl Acad*  
740 *Sci U S A* **117**, 15036-15046, doi:10.1073/pnas.2001521117 (2020).

741 30 Li, Y. *et al.* Transcription-coupled structural dynamics of topologically associating  
742 domains regulate replication origin efficiency. *Genome Biol* **22**, 206,  
743 doi:10.1186/s13059-021-02424-w (2021).

744 31 Du, Z. *et al.* Allelic reprogramming of 3D chromatin architecture during early  
745 mammalian development. *Nature* **547**, 232-235, doi:10.1038/nature23263 (2017).

746 32 Zhang, J. *et al.* DONSON and FANCM associate with different replisomes  
747 distinguished by replication timing and chromatin domain. *Nat Commun* **11**, 3951,  
748 doi:10.1038/s41467-020-17449-1 (2020).

749 33 Porkka, K. P., Tammela, T. L., Vessella, R. L. & Visakorpi, T. RAD21 and KIAA0196  
750 at 8q24 are amplified and overexpressed in prostate cancer. *Genes Chromosomes*  
751 *Cancer* **39**, 1-10, doi:10.1002/gcc.10289 (2004).

752 34 Xu, H. *et al.* Enhanced RAD21 cohesin expression confers poor prognosis and  
753 resistance to chemotherapy in high grade luminal, basal and HER2 breast cancers.  
754 *Breast Cancer Res* **13**, R9, doi:10.1186/bcr2814 (2011).

755 35 Atienza, J. M. *et al.* Suppression of RAD21 gene expression decreases cell growth  
756 and enhances cytotoxicity of etoposide and bleomycin in human breast cancer cells.  
757 *Mol Cancer Ther* **4**, 361-368, doi:10.1158/1535-7163.MCT-04-0241 (2005).

758 36 Sonnessa, M. *et al.* NLRP3 Inflammasome From Bench to Bedside: New  
759 Perspectives for Triple Negative Breast Cancer. *Frontiers in Oncology* **10**, doi:ARTN  
760 158710.3389/fonc.2020.01587 (2020).

761 37 Wang, L. M. *et al.* Identification of Alternatively-Activated Pathways between  
762 Primary Breast Cancer and Liver Metastatic Cancer Using Microarray Data.

763 *Genes-Basel* **10**, doi:ARTN 75310.3390/genes10100753 (2019).

764 38 Cruceriu, D., Baldasici, O., Balacescu, O. & Berindan-Neagoe, I. The dual role of  
765 tumor necrosis factor-alpha (TNF-alpha) in breast cancer: molecular insights and  
766 therapeutic approaches. *Cell Oncol* **43**, 1-18, doi:10.1007/s13402-019-00489-1  
767 (2020).

768 39 Chen, Y., Li, L. H. & Zhang, J. F. Cell migration inducing hyaluronidase 1 (CEMIP)  
769 activates STAT3 pathway to facilitate cell proliferation and migration in breast cancer.  
770 *J Recept Sig Transd* **41**, 145-152, doi:10.1080/10799893.2020.1800732 (2021).

771 40 Banach, A. *et al.* CEMIP upregulates BiP to promote breast cancer cell survival in  
772 hypoxia. *Oncotarget* **10**, 4307-4320, doi:10.18632/oncotarget.27036 (2019).

773 41 Xu, J. *et al.* Association between KIAA1199 overexpression and tumor invasion,  
774 TNM stage, and poor prognosis in colorectal cancer. *Int J Clin Exp Patho* **8**,  
775 2909-2918 (2015).

776 42 Gillespie, P. J. & Hirano, T. Scc2 couples replication licensing to sister chromatid  
777 cohesion in *Xenopus* egg extracts. *Curr Biol* **14**, 1598-1603,  
778 doi:10.1016/j.cub.2004.07.053 (2004).

779 43 Lengronne, A. *et al.* Cohesin relocation from sites of chromosomal loading to places  
780 of convergent transcription. *Nature* **430**, 573-578, doi:10.1038/nature02742 (2004).

781 44 Watrin, E. *et al.* Human Scc4 is required for cohesin binding to chromatin,  
782 sister-chromatid cohesion, and mitotic progression. *Current Biology* **16**, 863-874,  
783 doi:10.1016/j.cub.2006.03.049 (2006).

784 45 Kikuchi, S., Borek, D. M., Otwinowski, Z., Tomchick, D. R. & Yu, H. Crystal

785 structure of the cohesin loader Scc2 and insight into cohesinopathy. *Proc Natl Acad*  
786 *Sci U S A* **113**, 12444-12449, doi:10.1073/pnas.1611333113 (2016).

787 46 Hansen, A. S., Pustova, I., Cattoglio, C., Tjian, R. & Darzacq, X. CTCF and cohesin  
788 regulate chromatin loop stability with distinct dynamics. *eLife* **6**,  
789 doi:10.7554/eLife.25776 (2017).

790 47 Bonev, B. & Cavalli, G. Organization and function of the 3D genome. *Nat Rev Genet*  
791 **17**, 661-678, doi:10.1038/nrg.2016.112 (2016).

792 48 Michaelis, C., Ciosk, R. & Nasmyth, K. Cohesins: Chromosomal proteins that  
793 prevent premature separation of sister chromatids. *Cell* **91**, 35-45, doi:Doi  
794 10.1016/S0092-8674(01)80007-6 (1997).

795 49 Weitzer, S., Lehane, C. & Uhlmann, F. A model for ATP hydrolysis-dependent  
796 binding of cohesin to DNA. *Curr Biol* **13**, 1930-1940, doi:10.1016/j.cub.2003.10.030  
797 (2003).

798 50 Ryu, J. K. *et al.* Bridging-induced phase separation induced by cohesin SMC protein  
799 complexes. *Sci Adv* **7**, doi:10.1126/sciadv.abe5905 (2021).

800 51 Shao, S. *et al.* TagBiFC technique allows long-term single-molecule tracking of  
801 protein-protein interactions in living cells. *Commun Biol* **4**, 378,  
802 doi:10.1038/s42003-021-01896-7 (2021).

803 52 Boettiger, A. N. *et al.* Super-resolution imaging reveals distinct chromatin folding for  
804 different epigenetic states. *Nature* **529**, 418-422, doi:10.1038/nature16496 (2016).

805 53 Servant, N. *et al.* HiC-Pro: an optimized and flexible pipeline for Hi-C data  
806 processing. *Genome Biology* **16**, doi:ARTN 25910.1186/s13059-015-0831-x (2015).

807 54 Servant, N. *et al.* HiTC: exploration of high-throughput 'C' experiments.  
808 *Bioinformatics* **28**, 2843-2844, doi:10.1093/bioinformatics/bts521 (2012).

809 55 Crane, E. *et al.* Condensin-driven remodelling of X chromosome topology during  
810 dosage compensation. *Nature* **523**, 240-U299, doi:10.1038/nature14450 (2015).

811 56 van der Weide, R. H. *et al.* Hi-C analyses with GENOVA: a case study with cohesin  
812 variants. *NAR Genom Bioinform* **3**, lqab040, doi:10.1093/nargab/lqab040 (2021).

813 57 Flyamer, I. M., Illingworth, R. S. & Bickmore, W. A. Coolpup.py: versatile pile-up  
814 analysis of Hi-C data. *Bioinformatics* **36**, 2980-2985,  
815 doi:10.1093/bioinformatics/btaa073 (2020).

816 58 Quinlan, A. R. BEDTools: The Swiss-Army Tool for Genome Feature Analysis. *Curr*  
817 *Protoc Bioinformatics* **47**, 11 12 11-34, doi:10.1002/0471250953.bi1112s47 (2014).

818 59 Anders, S., Pyl, P. T. & Huber, W. HTSeq--a Python framework to work with  
819 high-throughput sequencing data. *Bioinformatics* **31**, 166-169,  
820 doi:10.1093/bioinformatics/btu638 (2015).

821 60 Love, M. I., Huber, W. & Anders, S. Moderated estimation of fold change and  
822 dispersion for RNA-seq data with DESeq2. *Genome Biol* **15**, 550,  
823 doi:10.1186/s13059-014-0550-8 (2014).

824 61 Mootha, V. K. *et al.* PGC-1alpha-responsive genes involved in oxidative  
825 phosphorylation are coordinately downregulated in human diabetes. *Nature genetics*  
826 **34**, 267-273, doi:10.1038/ng1180 (2003).

827 62 Subramanian, A. *et al.* Gene set enrichment analysis: a knowledge-based approach for  
828 interpreting genome-wide expression profiles. *Proc Natl Acad Sci U S A* **102**,

829 15545-15550, doi:10.1073/pnas.0506580102 (2005).

830 63 Kuleshov, M. V. *et al.* Enrichr: a comprehensive gene set enrichment analysis web  
831 server 2016 update. *Nucleic Acids Res* **44**, W90-97, doi:10.1093/nar/gkw377 (2016).

832

### 833 **Figure legends**

834 **Fig. 1 Cohesin is arranged in axial chromosomal domains in cells with up-regulated**  
835 **Rad21.**

836 **a** Super-resolution images of HeLa cell transfected with human Rad21. Scare bar, 5  $\mu$ m.  
837 Right, higher magnification of vermicelli. Scare bar, 1  $\mu$ m.

838 **b** Histogram of bead-to-bead distance along the vermicelli fiber in Rad21 over-expressed  
839 cell (n=210).

840 **c** Live cell super-resolution images of vermicelli morphology in cells with different after  
841 transfected over different time. Scare bar, 5  $\mu$ m.

842 **d** Plots compare mean intensity (y axis) and heterogenetic level (x axis) after Rad21  
843 up-regulation for different time (n > 36 per condition).

844 **e** Representative images of an inverse fluorescence recovery after photobleaching (iFRAP)  
845 assay of Rad21-OE in HeLa cells. Scare bar, 5  $\mu$ m.

846 **f** The fluorescence signals of unbleached regions were normalized to the first pre-bleach  
847 image and plotted (mean  $\pm$  S.D., n = 14 per condition).

848 **g** Super-resolution images of cohesin subunits in the absence or presence of Rad21  
849 over-expression labelled with antibodies. Scare bar, 5  $\mu$ m.

850 **h** Colocalization analysis of vermicelli and protein in (G) (n $\approx$ 40 per condition). The lower  
851 quartile, median and upper quartile values were labelled in the box.

852 **i** Live cell super-resolution images of three Rad21 mutants in (Supplementary information,  
853 Fig. S4b) over-expressed in HeLa cell. Scale bar, 5  $\mu$ m.

854

855 **Fig. 2 NIPBL-Rad21 interaction facilitates vermicelli formation by promoting cohesin**  
856 **loading.**

857 **a** Proteins extracted sequentially at different salt (NaCl) concentrations were  
858 immunoblotted with antibodies specific for Rad21, SMC3, H3 or ACTB.

859 **b** The distribution of Rad21 and SMC3 detected in the Western blot shown in A was  
860 quantified and normalized to the amount of ACTB and H3. The sample volumes are 1:  
861 0.5: 0.4 (0.1M: 0.5M: 1M).

862 **c** Co-immunoprecipitation and immunoblot assay against SMC3 detect cohesin formation  
863 with endogenous Rad21, wild-type Rad21-OE.

864 **d** Co-immunoprecipitation and immunoblot assay against SMC3 detect cohesin loading  
865 with endogenous Rad21, wild-type or LIS-Ala-mutant Rad21-OE.

866 **e** Representative images of FRAP assay of HeLa cells transfected with LIS-Ala-mutant  
867 Rad21 (scare bar is 5  $\mu$ m).

868 **f** The fluorescence signals of unbleached regions were normalized to the first pre bleach  
869 image and plotted (mean  $\pm$  S.D., n = 14 per condition).

870 **g** Super-resolution images of cohesin subunits in the absence of Rad21 and  
871 wild-type/LIS-Ala SMC1A or SMC3 over-expression. Scare bar, 5  $\mu$ m.

872

873 **Fig. 3 CTCF anchored excessive cohesin saddle on topologically associated domains**  
874 **(TADs).**

875 **a** Super-resolution images of H2B, CTCF, NIPBL, MAU2 in the absence or presence of  
876 Rad21 over-expression labelled with antibodies. Scare bar, 5  $\mu\text{m}$ .

877 **b** Co-localization analysis of vermicelli and protein in (A) ( $n\approx 40$  per condition). The lower  
878 quartile, median and upper quartile values were labelled in the box.

879 **c** Co-localization ratio of CTCT and Rad21 in the presence of Rad21 over-expression ( $n=$   
880 54 per condition).

881 **d** Super-resolution images of EMC7 TAD in the absence or presence of Rad21  
882 over-expression labelled by *in situ* hybridization with DNA probes. Scare bar, 5  $\mu\text{m}$ .  
883 Boxed regions are shown as magnified inserts. Scare bar, 1  $\mu\text{m}$ .

884 **e** The normalized intensity profile of boxed region in G measured across the center of the  
885 EMC TAD and Rad21 ( $n=20$  per condition).

886 **f** Scheme of proposed cohesin-mediated loop model.

887 **g** Quantification of volume change of EMC7 TADs after Rad21 over-expression. ( $n>380$   
888 per condition). The lower quartile, median and upper quartile values were labelled in the  
889 box.

890 **h** Example images of chromosome territory (CT) 2 in Rad21 over-expressed HeLa cell  
891 obtained by CT2 probes, JF549 and DAPI. Scare bar, 5  $\mu\text{m}$ .

892 **i** Quantification of morphology change of CT2 by calculating the radius of gyration ( $n=77$   
893 per condition).

894

895 **Fig. 4 Rad21-OE stimulates cohesin activity affecting genome contacts.**

- 896 **a** Hi-C interaction frequency as a function of logarithmically increasing genomic distance  
897 bins for cells with and without Rad21 over-expression
- 898 **b** Hi-C contact matrices of chromosome 2 (0-100Mb) in control and Rad21-OE HeLa cells.  
899 Direct minus between Rad21-OE and control matrices is on the right.
- 900 **c** Normalized Hi-C interaction matrices for chromosome 5 (80–160 Mb) in control and  
901 Rad21-OE cells, and differential matrices of genomic regions between control and  
902 Rad21-OE cells (resolution: 150 kb). Below the heatmaps are PC1 values and gene  
903 density plots. Orange represents compartment A and blue represents compartment B.  
904 High gene density regions correlate with compartment A.
- 905 **d** Ratios of inter-compartment interactions (AB) and intra-compartment interactions  
906 (AA+BB) for each chromosome (X chromosome excluded) in control and Rad21-OE  
907 cells (\*\*P < 0.001, wilcoxon.test).
- 908 **e** Average contact frequency enrichment showing the extent of compartmentalization in  
909 control and Rad21-OE cells. Direct minus between Rad21-OE and control matrices is on  
910 the bottom-right.
- 911 **f** Genome-wide summary of genomic regions switching between A/B compartments in  
912 control and Rad21-OE cells.
- 913 **g** Example immunofluorescence images of control and Rad21 over-expression HeLa cells  
914 using anti-H3K27me3(Green) and H3K4me3(Red) (scale bar is 5  $\mu$ m).
- 915 **h** Example immunofluorescence images of control and Rad21 over-expression HeLa cells  
916 using anti-HP1 $\alpha$ (Red) (scale bar is 5  $\mu$ m).
- 917 **i** Hi-C contact matrices for a zoomed in region on chromosome 2. Matrices are normalized  
918 to 160 million contacts, shown resolution is 40 kb. IS, insulation score, shows TAD  
919 pattern and insulation score distribution. Above and to the left of the contact matrices the  
920 union of CTCF sites identified in wild-type are shown. Red and blue triangles denote  
921 forward and reverse CTCF sites, respectively. Black histogram is CTCF ChIP-seq of  
922 wild-type HeLa.
- 923 **j** Aggregate TAD analysis (ATA) calculates the average Hi-C signal across a selected set  
924 of TADs. The differential ATA signal between Rad21-OE and control is visualized for all  
925 TADs in the size range >200kb. Blue indicates a higher signal in the control, red  
926 indicates a higher signal in Rad21-OE cells.
- 927 **k** Contact frequency ratio of intra-TAD and inter-TAD (TAD score) (\*\*P < 0.001, paired  
928 t-test).

929

930 **Fig. 5 Rad21 up-regulation results in oncogenic behaviors of breast cancer by regulating**  
931 **genomic structure.**

- 932 **a** The survival plot based on the expression of Rad21 (orange line denotes the high  
933 expression group; blue line denotes the low expression group).
- 934 **b** Gene expression of Rad21 in breast cancer and normal samples from TCGA database.
- 935 **c** Example live cell super-resolution images of MCF10A, MDA-MB-157, SK-BR-3 and  
936 HCC1395 cells. Scale bar, 5  $\mu$ m.
- 937 **d** Extent of Rad21 clustering after overexpressed in HeLa cell from (A) were quantified by  
938 heterogenous level (n > 30 per condition). The lower quartile, median and upper quartile  
939 values were labelled in the box.
- 940 **e** Heatmap showing differentially expressed genes (p < 0.05, Benjamini-Hochberg; log<sub>2</sub>  
941 Fold change >1 or log<sub>2</sub> Fold change <-1) in Rad21-OE cells vs. control cells. Some  
942 marker genes associated with breast cancer were shown in the right of heatmap.
- 943 **f** Above: Boxplots showing gene expression changes in regions with compartment  
944 switching compared to the stable. P-values: Wilcoxon rank-sum test. Bottom: An  
945 example of expression level changes of cancer related genes (IL7R) in the regions from  
946 B to A compartments upon Rad21 over-expression.
- 947 **g** Quantification of the difference of TAD score between Rad21-OE and control. P-values:  
948 Wilcoxon rank-sum test. (TAD score= intra-TAD / inter-TAD)

949

950 **Fig. 6 A model illustrating the role of Rad21 as a core subunit of cohesin to extrude DNA**  
951 **and facilitate formation of high-order chromatin structure, under normal expression**  
952 **level (left panel) and high expression level (right panel) of Rad21.**

953 **a** Rad21 up-regulation causes excessive chromatin condensation with a vermicelli-like  
954 morphology.

955 **b** Up-regulated Rad21 facilitates cohesin loading by enhancing the interactions with  
956 cohesin loader, overloaded cohesin extrude more chromatin loops and become more  
957 aggregated.

958 **c** At a larger scale, the Rad21 aggregate into cluster, which is located at the middle of a  
959 TAD.

960 **d** Up-regulated Rad21 leads to increase inter-TAD interaction.

961 **e** At the subchromosome scale, the A and B compartments are less segregated after Rad21  
962 up-regulation.

Fig. 1

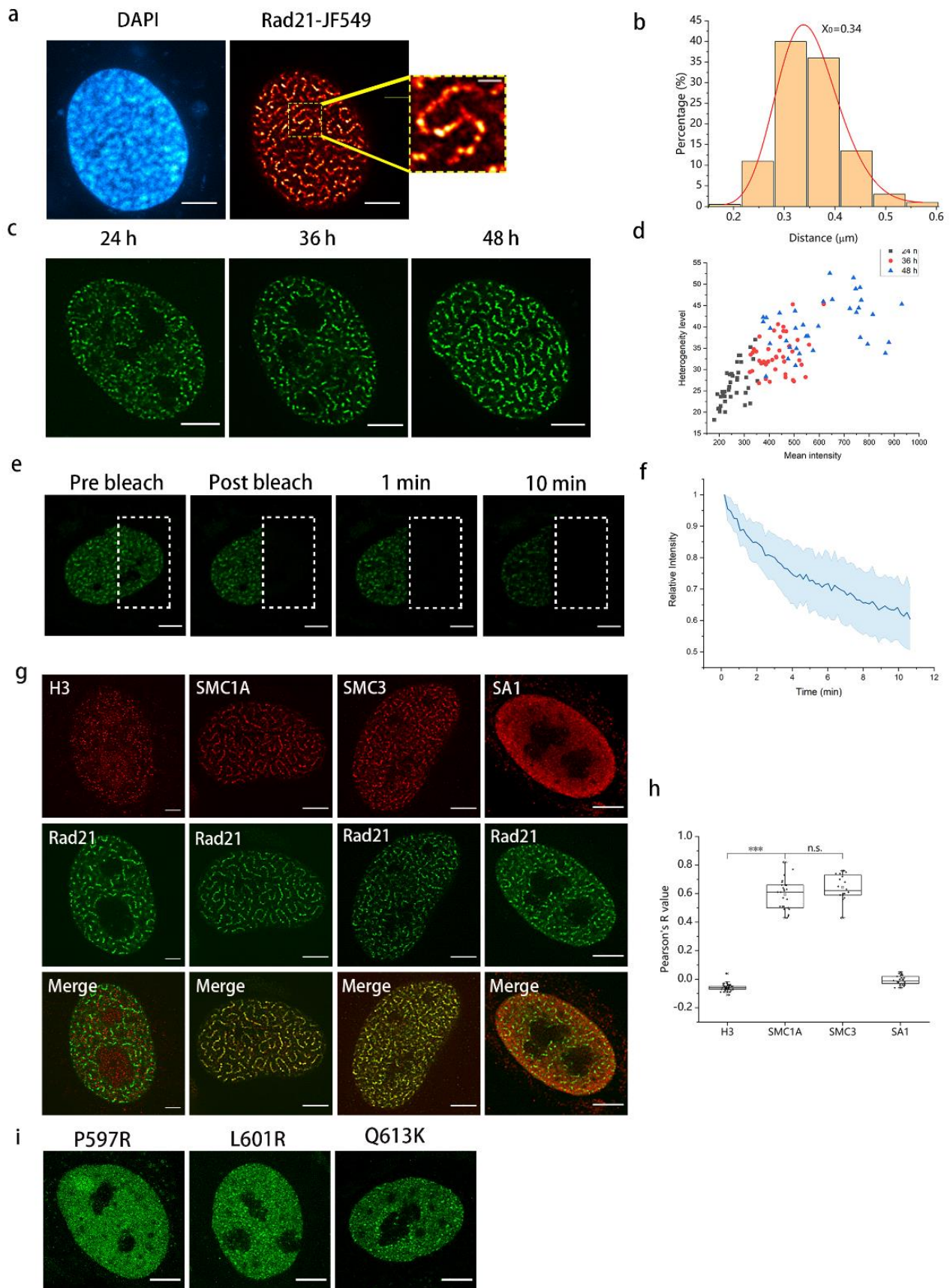


**Fig. 2**

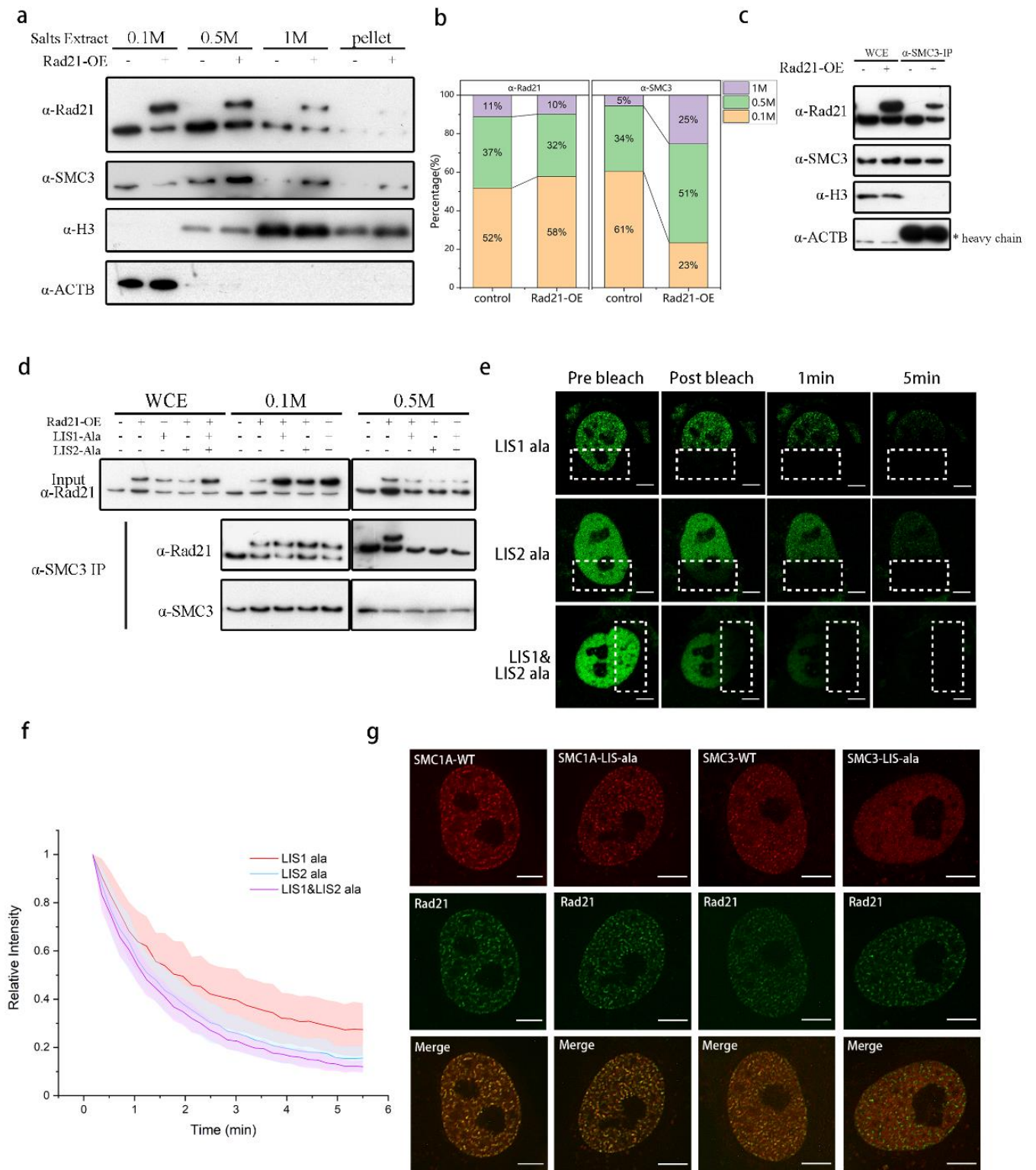
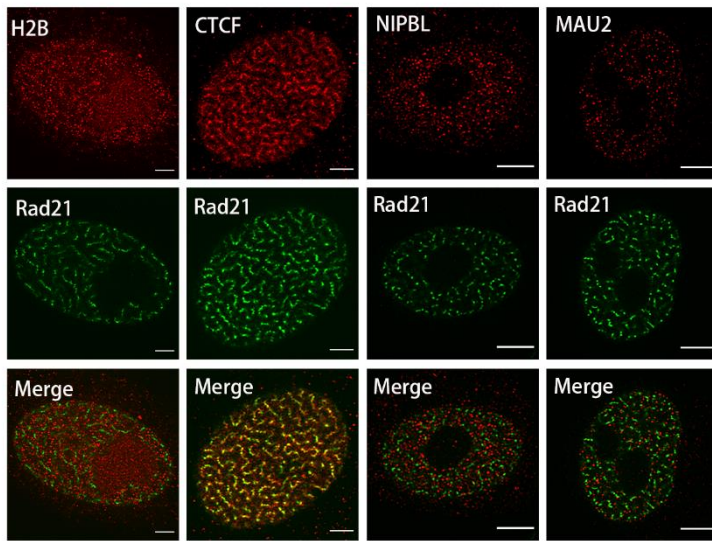
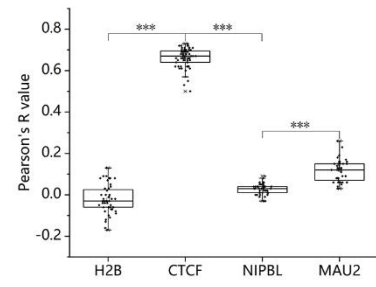
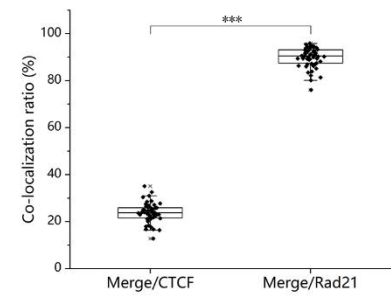
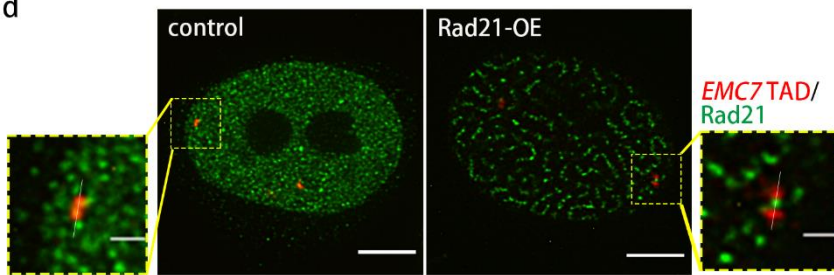
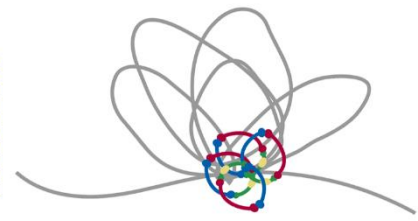
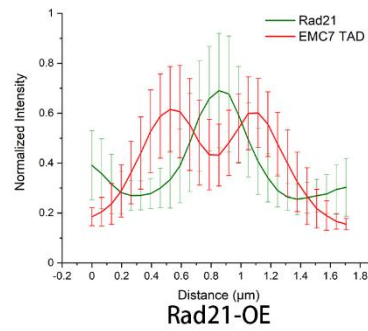
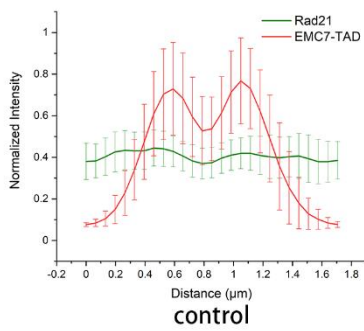
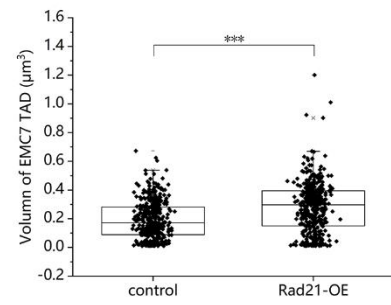
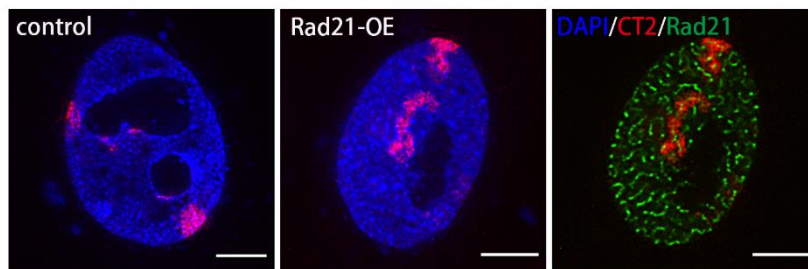
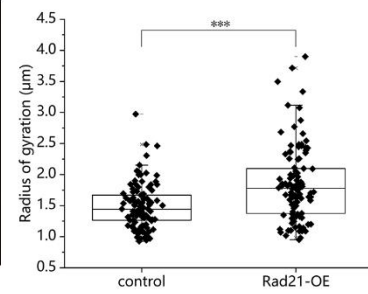
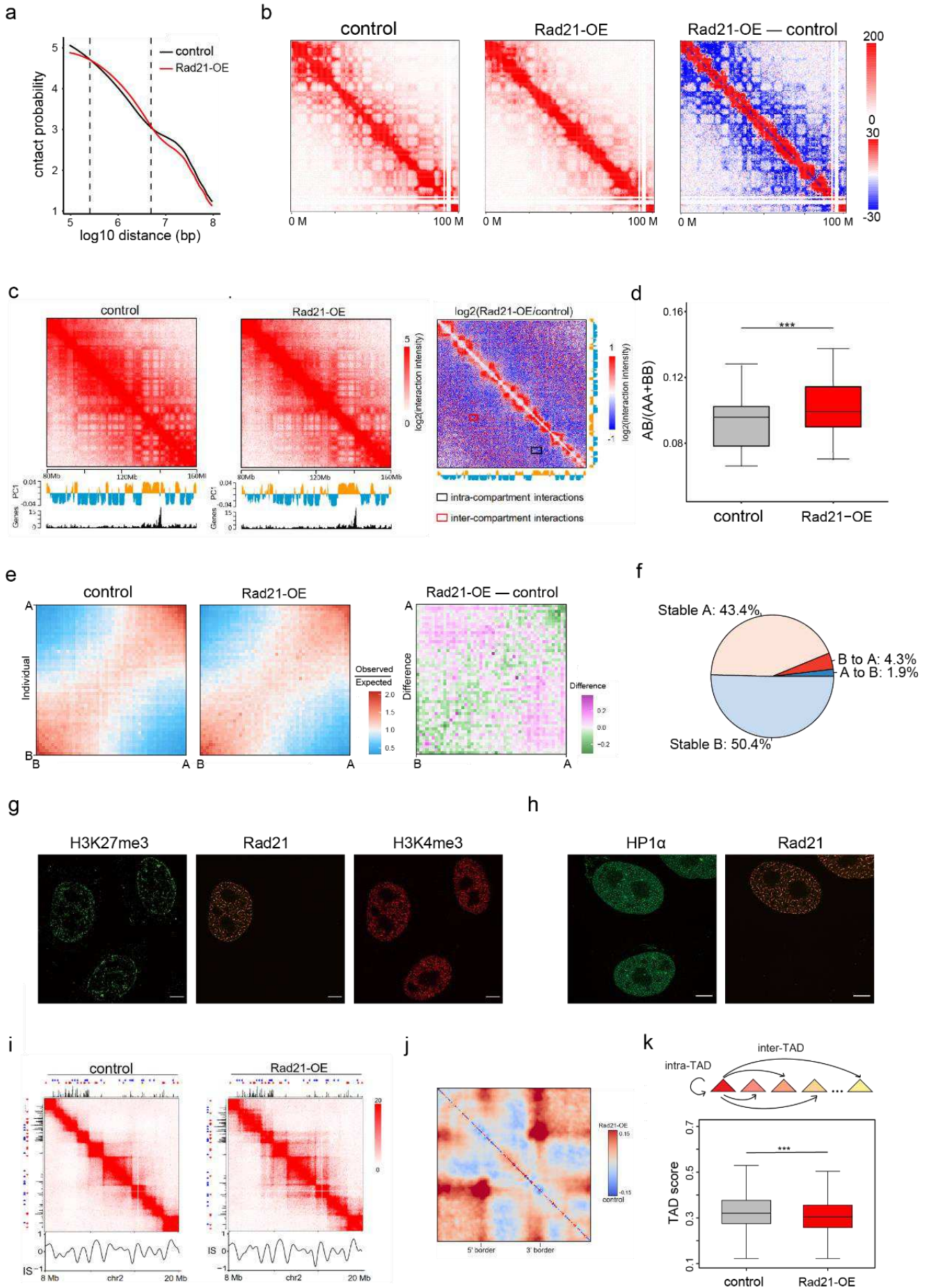


Fig. 3

**a****b****c****d****f****e****g****h****i**

**Fig. 4**



**Fig. 5**

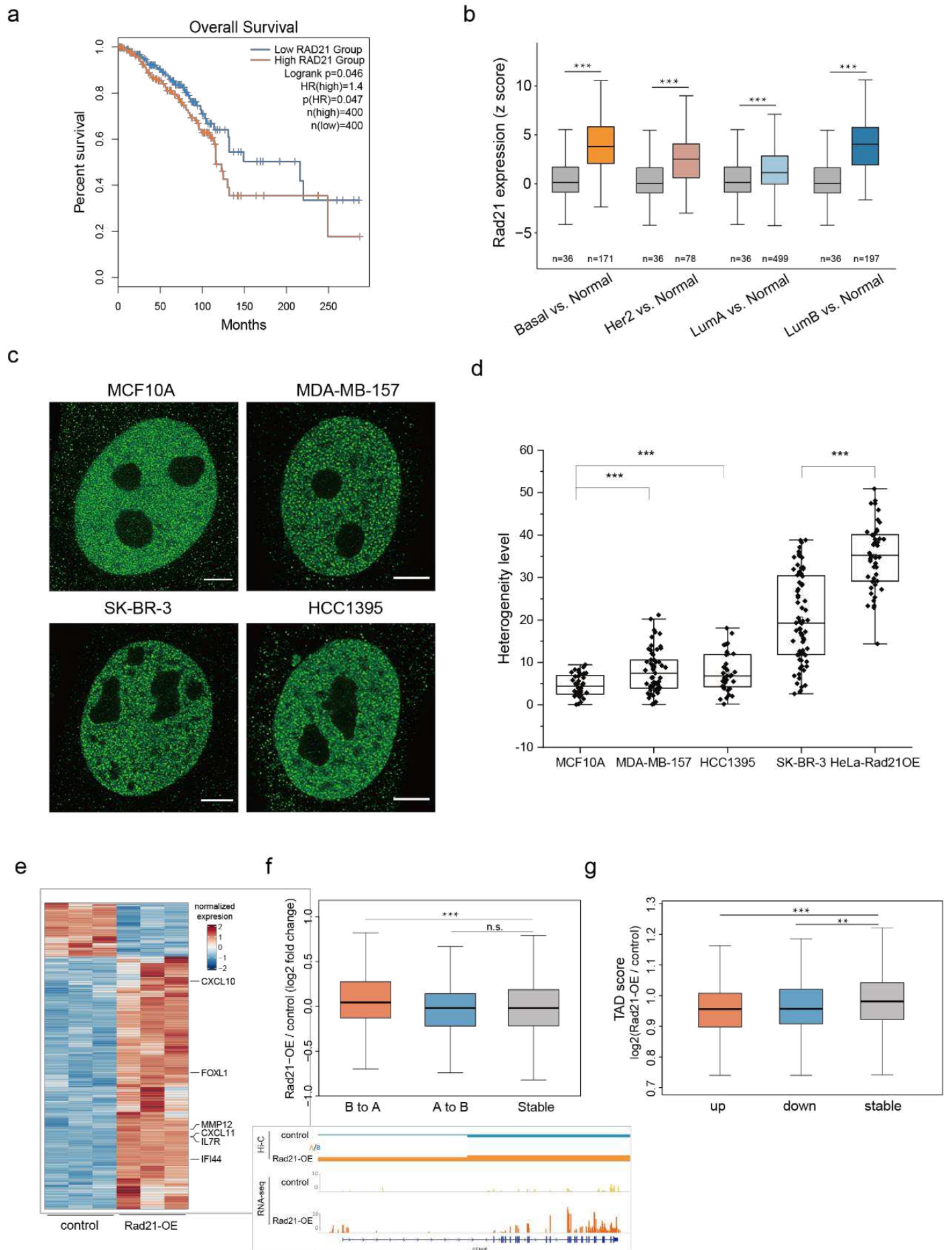
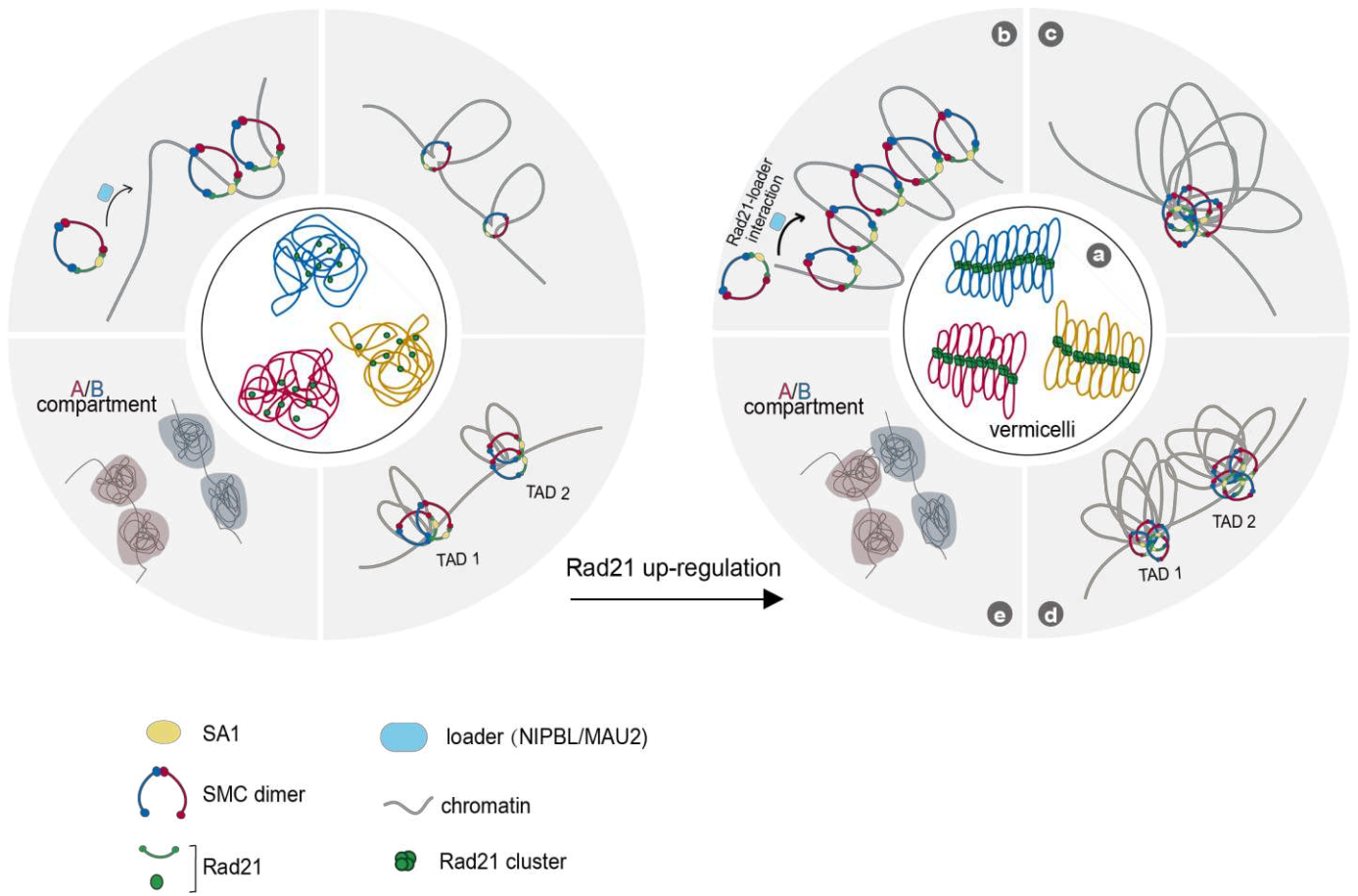
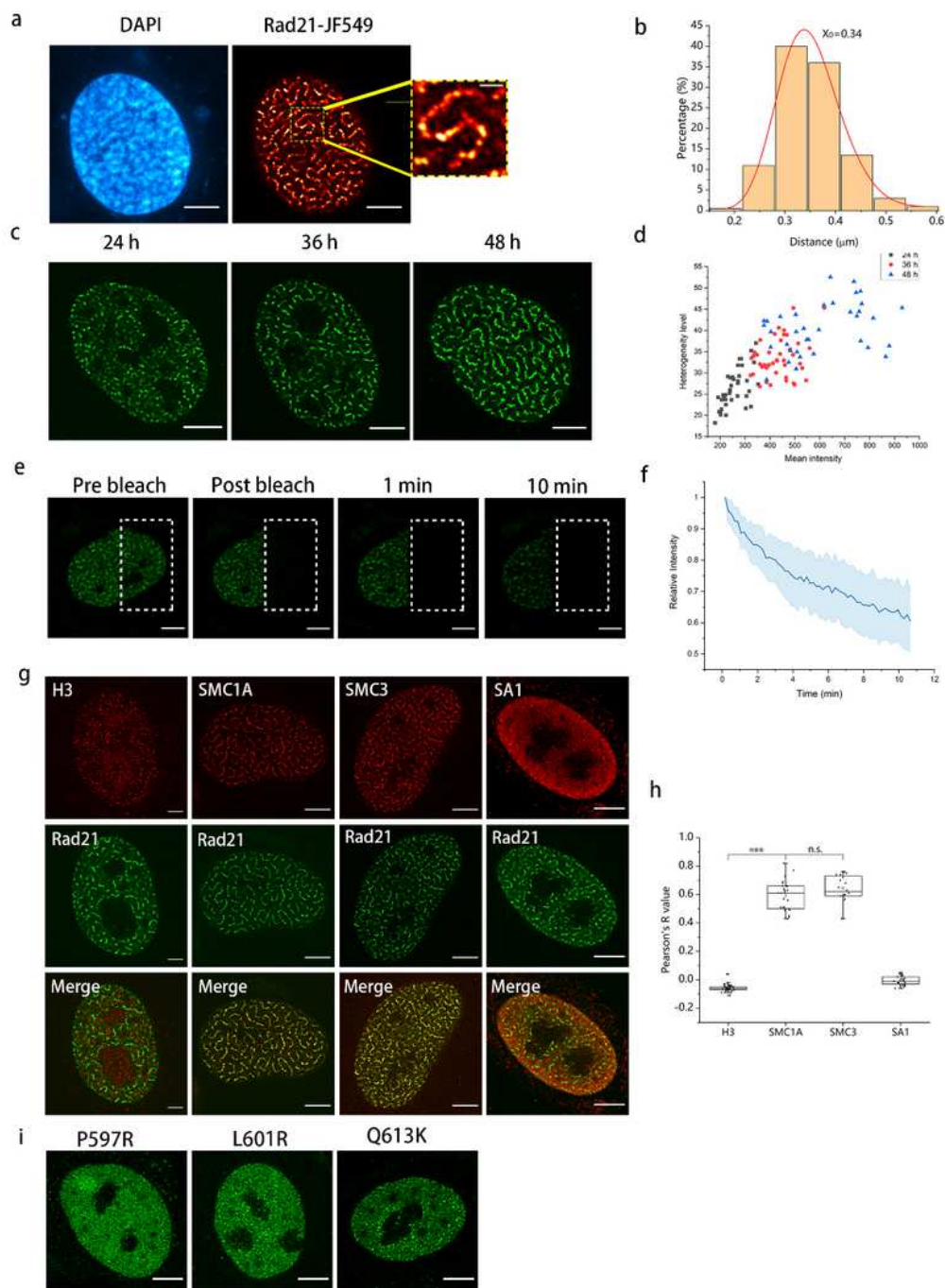


Fig. 6



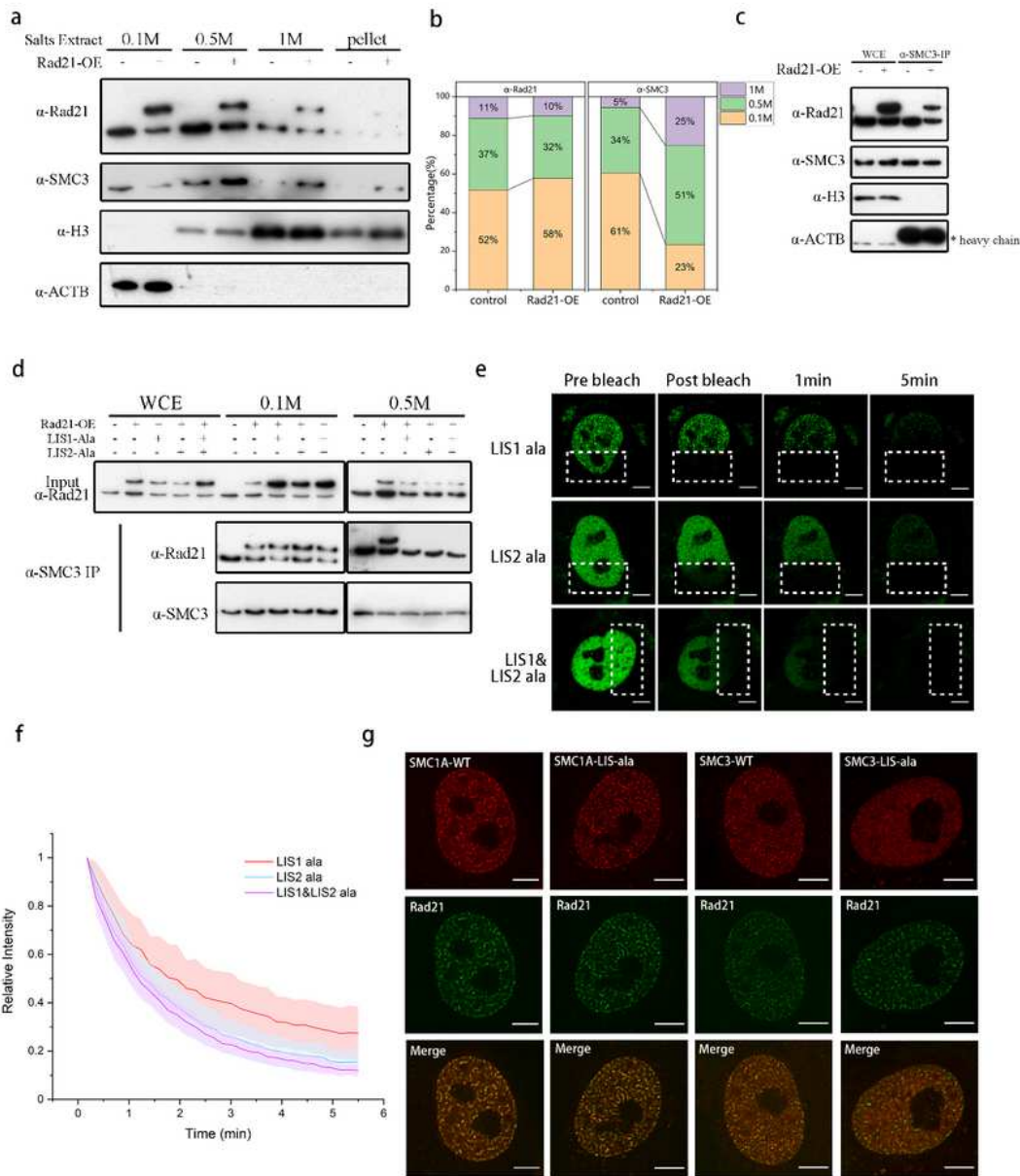
# Figures



**Figure 1**

Cohesin is arranged in axial chromosomal domains in cells with up-regulated Rad21. a Super-resolution images of HeLa cell transfected with human Rad21. Scare bar, 5  $\mu\text{m}$ . Right, higher magnification of vermicelli. Scare bar, 1  $\mu\text{m}$ . b Histogram of bead-to-bead distance along the vermicelli fiber in Rad21 over-

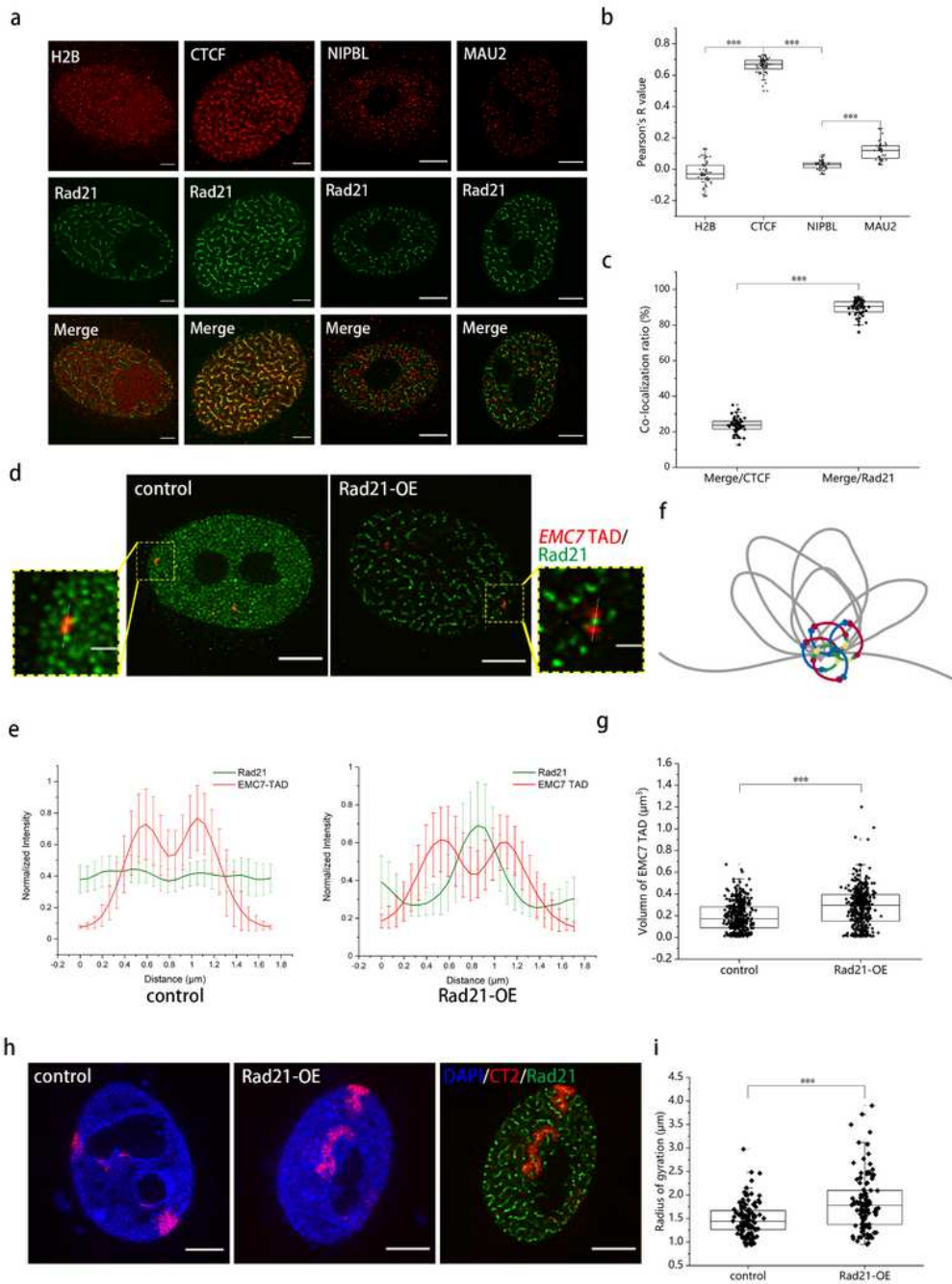
expressed cell (n=210). c Live cell super-resolution images of vermicelli morphology in cells with different after transfected over different time. Scare bar, 5  $\mu\text{m}$ . d Plots compare mean intensity (y axis) and heterogenetic level (x axis) after Rad21 up-regulation for different time (n $\approx$ 36 per condition). e Representative images of an inverse fluorescence recovery after photobleaching (iFRAP) assay of Rad21-OE in HeLa cells. Scare bar, 5  $\mu\text{m}$ . f The fluorescence signals of unbleached regions were normalized to the first pre-bleach image and plotted (mean  $\pm$  S.D., n = 14 per condition). g Super-resolution images of cohesin subunits in the absence or presence of Rad21 over-expression labelled with antibodies. Scare bar, 5  $\mu\text{m}$ . h Colocalization analysis of vermicelli and protein in (G) (n $\approx$ 40 per condition). The lower quartile, median and upper quartile values were labelled in the box. i Live cell super-resolution images of three Rad21 mutants in (Supplementary information, Fig. S4b) over-expressed in HeLa cell. Scale bar, 5  $\mu\text{m}$ .



**Figure 2**

NIPBL-Rad21 interaction facilitates vermicelli formation by promoting cohesin loading. **a** Proteins extracted sequentially at different salt (NaCl) concentrations were immunoblotted with antibodies specific for Rad21, SMC3, H3 or ACTB. **b** The distribution of Rad21 and SMC3 detected in the Western blot shown in **A** was quantified and normalized to the amount of ACTB and H3. The sample volumes are 1: 0.5: 0.4 (0.1M: 0.5M: 1M). **c** Co-immunoprecipitation and immunoblot assay against SMC3 detect

cohesin formation with endogenous Rad21, wild-type Rad21-OE. d Co-immunoprecipitation and immunoblot assay against SMC3 detect cohesin loading with endogenous Rad21, wild-type or LIS-Ala-mutant Rad21-OE. e Representative images of FRAP assay of HeLa cells transfected with LIS-Ala-mutant Rad21 (scare bar is 5  $\mu\text{m}$ ). f The fluorescence signals of unbleached regions were normalized to the first pre bleach image and plotted (mean  $\pm$  S.D.,  $n = 14$  per condition). g Super-resolution images of cohesin subunits in the absence of Rad21 and wild-type/LIS-Ala SMC1A or SMC3 over-expression. Scare bar, 5  $\mu\text{m}$ .

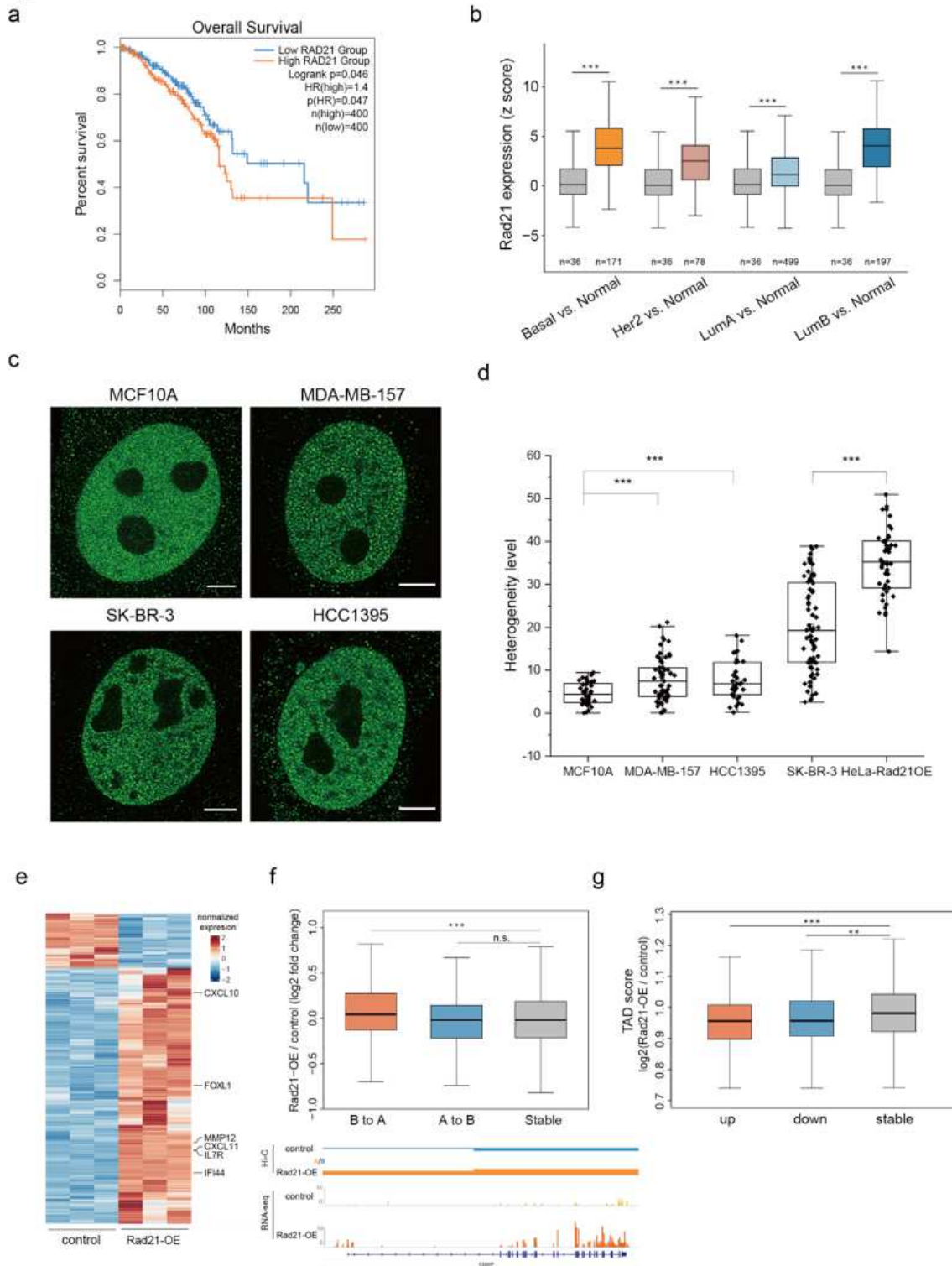


### Figure 3

CTCF anchored excessive cohesin saddle on topologically associated domains (TADs). a Super-resolution images of H2B, CTCF, NIPBL, MAU2 in the absence or presence of Rad21 over-expression labelled with antibodies. Scare bar, 5  $\mu\text{m}$ . b Co-localization analysis of vermicelli and protein in (A) ( $n \approx 40$  per condition). The lower quartile, median and upper quartile values were labelled in the box. c Co-localization ratio of CTCT and Rad21 in the presence of Rad21 over-expression ( $n = 54$  per condition). d Super-resolution images of EMC7 TAD in the absence or presence of Rad21 over-expression labelled by in situ hybridization with DNA probes. Scare bar, 5  $\mu\text{m}$ . Boxed regions are shown as magnified inserts. Scare bar, 1  $\mu\text{m}$ . e The normalized intensity profile of boxed region in G measured across the center of the EMC TAD and Rad21 ( $n = 20$  per condition). f Scheme of proposed cohesin-mediated loop model. g Quantification of volume change of EMC7 TADs after Rad21 over-expression. ( $n > 380$  per condition). The lower quartile, median and upper quartile values were labelled in the box. h Example images of chromosome territory (CT) 2 in Rad21 over-expressed HeLa cell obtained by CT2 probes, JF549 and DAPI. Scare bar, 5  $\mu\text{m}$ . i Quantification of morphology change of CT2 by calculating the radius of gyration ( $n = 77$  per condition).



genomic regions between control and Rad21-OE cells (resolution: 150 kb). Below the heatmaps are PC1 values and gene density plots. Orange represents compartment A and blue represents compartment B. High gene density regions correlate with compartment A. d Ratios of inter-compartment interactions (AB) and intra-compartment interactions (AA+BB) for each chromosome (X chromosome excluded) in control and Rad21-OE cells (\*\*P < 0.01, wilcoxon.test). e Average contact frequency enrichment showing the extent of compartmentalization in control and Rad21-OE cells. Direct minus between Rad21-OE and control matrices is on the bottom-right. f Genome-wide summary of genomic regions switching between A/B compartments in control and Rad21-OE cells. g Example immunofluorescence images of control and Rad21 over-expression HeLa cells using anti-H3K27me3(Green) and H3K4me3(Red) (scale bar is 5  $\mu$ m). h Example immunofluorescence images of control and Rad21 over-expression HeLa cells using anti-HP1 $\alpha$ (Red) (scale bar is 5  $\mu$ m). i Hi-C contact matrices for a zoomed in region on chromosome 2. Matrices are normalized to 160 million contacts, shown resolution is 40 kb. IS, insulation score, shows TAD pattern and insulation score distribution. Above and to the left of the contact matrices the union of CTCF sites identified in wild-type are shown. Red and blue triangles denote forward and reverse CTCF sites, respectively. Black histogram is CTCF ChIP-seq of wild-type HeLa. j Aggregate TAD analysis (ATA) calculates the average Hi-C signal across a selected set of TADs. The differential ATA signal between Rad21-OE and control is visualized for all TADs in the size range >200kb. Blue indicates a higher signal in the control, red indicates a higher signal in Rad21-OE cells. k Contact frequency ratio of intra-TAD and inter-TAD (TAD score) (\*\*P < 0.01, paired t-test).

**Fig. 5****Figure 5**

Rad21 up-regulation results in oncogenic behaviors of breast cancer by regulating genomic structure. a The survival plot based on the expression of Rad21 (orange line denotes the high expression group; blue line denotes the low expression group). b Gene expression of Rad21 in breast cancer and normal samples from TCGA database. c Example live cell super-resolution images of MCF10A, MDA-MB-157, SK-BR-3 and HCC1395 cells. Scale bar, 5  $\mu\text{m}$ . d Extent of Rad21 clustering after overexpressed in HeLa cell from (A)

were quantified by heterogenetic level ( $n \geq 30$  per condition). The lower quartile, median and upper quartile values were labelled in the box. e Heatmap showing differentially expressed genes ( $p < 0.05$ , Benjamini-Hochberg;  $\log_2$  Fold change  $>1$  or  $\log_2$  Fold change  $<-1$ ) in Rad21-OE cells vs. control cells. Some marker genes associated with breast cancer were shown in the right of heatmap. f Above: Boxplots showing gene expression changes in regions with compartment switching compared to the stable. P-values: Wilcoxon rank-sum test. Bottom: An example of expression level changes of cancer related genes (IL7R) in the regions from B to A compartments upon Rad21 over-expression. g Quantification of the difference of TAD score between Rad21-OE and control. P-values: Wilcoxon rank-sum test. (TAD score= intra-TAD / inter-TAD)

**Fig. 6**

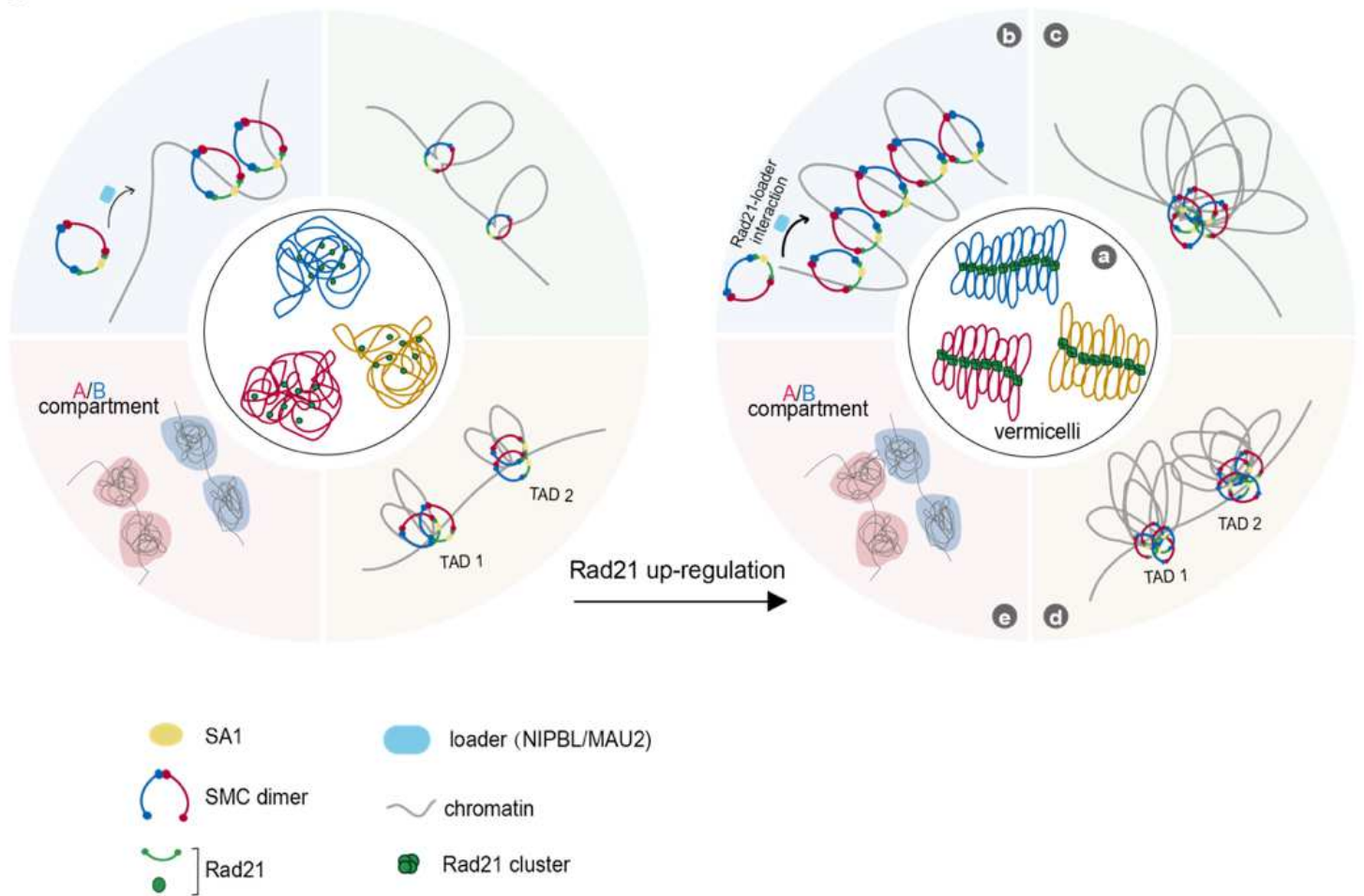


**Figure 6**

A model illustrating the role of Rad21 as a core subunit of cohesin to extrude DNA and facilitate formation of high-order chromatin structure, under normal expression level (left panel) and high expression level (right panel) of Rad21. a Rad21 up-regulation causes excessive chromatin condensation with a vermicelli-like morphology. b Up-regulated Rad21 facilitates cohesin loading by enhancing the interactions with cohesin loader, overloaded cohesin extrude more chromatin loops and become more aggregated. c At a larger scale, the Rad21 aggregate into cluster, which is located at the middle of a TAD.

d Up-regulated Rad21 leads to increase inter-TAD interaction. e At the subchromosome scale, the A and B compartments are less segregated after Rad21 up-regulation.

## Supplementary Files

This is a list of supplementary files associated with this preprint. Click to download.

- [20211118SupplementaryInformation.docx](#)
- [accessionnumbersandreviewertoken.pdf](#)
- [nrreportingsummaryflatten.pdf](#)